Journal of Wind Engineering & Industrial Aerodynamics xxx (xxxx) xxx-xxx

Contents lists available at ScienceDirect

Journal of Wind Engineering & Industrial Aerodynamics

journal homepage: http://ees.elsevier.com

Experimental investigation of the interaction between near-surface atmospheric boundary layer winds and downburst outflows

Djordje Romanic [a,bc,*], Horia Hangan [a]

[a] Wind Engineering, Energy and Environment (WindEEE) Research Institute, Western University, 2535 Advanced Avenue, London, Ontario, N6M 0E2, Canada
[b] Department of Civil, Chemical and Environmental Engineering (DICCA), Polytechnic School, University of Genoa, Via Montallegro 1, 16145, Genoa, Italy
[c] Department of Atmospheric and Oceanic Sciences, McGill University, Montréal, Québec, Canada

ARTICLE INFO

Keywords
Downbursts
Atmospheric boundary layer winds
Near-surface winds
Thunderstorms
Flow interaction
Physical experiments

ABSTRACT

This article focuses on experimental investigation of the interaction between downburst (DB) and near-surface atmospheric boundary layer (ABL) winds. The flow field of DB immersed into ABL winds (DBABL) is compared against the outflow produced by an isolated DB without ABL winds. The diameter of investigated downdrafts was 3.2 m. The study demonstrates that there is a profound difference between the radial velocity components in the DBABL and DB outflows in terms of peak and mean velocities, vertical profile of radial velocity, as well as the overall temporal signature of the velocity records. The asymmetry of the DBABL outflow in the along-ABL wind direction is similar to that observed in real traveling downbursts. The turbulence intensity in the near-surface DBABL winds can exceed 40% in some parts of the outflow where the downburst propagates against ABL winds. The DBABL wind profile is characterized by smaller nose-shape curvature than the DB winds in the part of the outflow where downburst and ABL winds have the same direction. The steady-state ABL wind segments and transient downburst segments in the DBABL velocity records are similar to anemometer records of real downbursts. The paper also shows that the velocity addition $\overline{\mathrm{DBABL}} \neq \overline{\mathrm{DB}} + \overline{\mathrm{ABL}}$ throughout the outflow.

1. Introduction

Downbursts are severe weather phenomena typically associated with thunderstorm clouds. Rain, hail, and graupel falling through and underneath a thunderstorm produce a downdraft of cold air that descends towards the ground. If the cloud base is high, the evaporation and melting of hydrometeors in the non-saturated environment additionally decrease the temperature of the falling air. Upon reaching the ground, the downdraft spreads horizontally and forms a starburst outflow pattern. This outflow plays an essential role in the structure, precipitation formation, and lifecycle of thunderstorms (Lompar et al., 2018), but can also produce damaging near-surface winds. For example, Fujita (1990) reported velocities as high as 75 m s^{-1} in intense microbursts (downbursts with the diameter of outflow below 4 km).

Using multi-Doppler radar observations from the Joint Airport Weather Studies (JAWS; Fujita, 1981), Wilson et al. (1984) and Hjelmfelt (1988) demonstrated that the thunderstorm cloud and the spawned downburst are not an isolated system, but instead both are embedded into the background atmospheric boundary layer (ABL) winds. In comparison to the thunderstorm cloud that is of the order of meso-γ scales (2–20 km), a background ABL wind is a larger scale phenomenon associated with, for instance, a cyclone or pressure depression. As a result, the thunderstorm cloud, as well as the resulting downburst, are constantly interacting with the ABL winds, as well as the wind aloft. The translating velocity of thunderstorm clouds is governed by the winds above the ABL and the winds in the upper portions of ABL (Bunkers et al., 2000).

The interaction between near-surface ABL winds and a downburst results in a more complex outflow than it would be if the downburst was an isolated phenomenon taking place in a calm environment (Mahoney, 1988). This complexity is observed after comparing radar images of full-scale downbursts (Wakimoto, 1982; Wilson et al., 1984; Hjelmfelt, 1988; Gunter and Schroeder, 2015) against flow fields of laboratory-produced gravity currents or impinging jets (Fairweather and Hargrave, 2002; Sengupta and Sarkar, 2008; Junayed et al., 2019). The complicated dynamics and environmental conditions associated with real downbursts makes it extremely challenging to estimate the contributions that an isolated downdraft, background ABL winds, and cloud translation have on the measured velocity at a given point in the outflow. Currently, there is no analytical formulation that in a satisfactory manner combines these three flow components, while the numerical simulations and physical experiments

* Corresponding author. Wind Engineering, Energy and Environment (WindEEE) Research Institute, Western University, 2535 Advanced Avenue, London, Ontario, N6M 0E2, Canada.
E-mail address: dromanic@uwo.ca (D. Romanic)

https://doi.org/10.1016/j.jweia.2020.104323
Received 18 April 2020; Received in revised form 13 July 2020; Accepted 25 July 2020
Available online xxx
0167-6105/© 2020.

are often overly idealized to properly capture the complex dynamics of real downburst outflows. The Doppler radar measurements by Hjelmfelt (1988) depict an asymmetric, nonhomogeneous and anisotropic wind field in the real downburst. However, these features are absent in downburst outflows produced without ABL winds in physical wind simulators (Sengupta and Sarkar, 2008; Junayed et al., 2019).

The interaction between downbursts and the environment has already been investigated in many numerical studies. Droegemeier and Wilhelmson (1987) analyzed the dynamics of thunderstorm outflows as a function of (1) the vertical temperature deficit profile, (2) the magnitude of the temperature deficit, and (3) the cold-air depth. Their numerical results showed that the outflow head depth and its propagation speed are mainly governed by the vertical temperature distribution in the atmosphere. Proctor (1988) modelled an isolated and stationary microburst in a three-dimensional (3D) and axisymmetric model. His comprehensive parametric study analyzed the sensitivity of microbursts to the environment and several other factors. In addition to some of the parameters previously examined in Droegemeier and Wilhelmson (1987), their study also analyzed the influence of precipitation characteristics on microburst outflows. A complex dynamics of colliding microbursts was studied in Anderson et al. (1992) using a 3D numerical model. Mason et al. (2009) and Mason et al. (2010) developed a sub-cloud model to analyze the sensitivity of downburst outflows to cooling source shape and its elevation, intensity, and topography. In particular, Mason et al. (2010) studied stationary and translating downdrafts in calm and sheared wind environments. Their results are in good agreement with the previous numerical work and full-scale data. The simulations of downdrafts embedded into ABL winds in Mason et al. (2010) were performed for two different ratios of ABL-to-downburst wind speed strengths. More discussion on Mason et al. (2010) is provided later in Section 4.1 when the present physical experiments are compared against their numerical results.

Most of the current wind simulators (e.g., Chay and Letchford, 2002; Sengupta and Sarkar, 2008; Xu and Hangan, 2008; McConville et al., 2009; Asano et al., 2019) are capable of physically simulating inclined downdrafts, pulsed jets, translating downdrafts, different downdraft diameters, and different nozzle heights above the impingement plane, but they are not designed to produce ABL winds and downburst-like impinging jets simultaneously. Two wind simulators that are presently capable of concurrently generating ABL winds and downbursts are the Wind Engineering, Energy and Environment (WindEEE) Dome (Hangan et al., 2017) at Western University in Canada, and the Laboratory of Building- and Environmental Aerodynamics at the Karlsruhe Institute of Technology in Germany.

When it comes to the latter of the two laboratories, Richter et al. (2018) investigated the interaction of impinging jets with the ambient flow in a street canyon using Particle Image Velocimetry (PIV). Their study was primarily focused on the influence of canyon orientation on a spread of the combined flows, and therefore the measured flow fields were highly influenced by the simulated buildings. Moreover, the diameter of their impinging jet upon reaching the canyon level was only 0.15–0.20 m, which at 1:200 geometric scale of their experiments, corresponds to a full-scale downdraft of 30–40 m. Moreover, the jet diameter at the nozzle exit was only 0.01 m. All considered, their study is more applicable to small-scale gusts than it is to thunderstorm downbursts whose diameters are above 400 m (Sengupta and Sarkar, 2008), and typically around 1500 m (Wilson et al., 1984; Hjelmfelt, 1988). Gromke and Ruck (2015) investigated the momentum transfer of the combined flows over the forest edge region. Two different forest edge configurations and several gusts of different durations were examined using PIV. Their study infers that the research targeted small scale downdraft-like gusts with a duration of 4–12 s, which is significantly below the time extent of real downbursts (Burlando et al., 2018; Zhang et al., 2018; Romanic et al., 2020a).

The WindEEE Dome is a large-scale wind simulator specifically designed to simulate downbursts and tornadoes (Hangan, 2010). The facility is also fully capable of producing ABL winds at different scales (Hangan et al., 2017). Junayed et al. (2019) characterized the mean and turbulence velocity fields of WindEEE Dome downbursts (without ABL winds) using point velocity measurements as well as PIV. A unique capability of the WindEEE Dome, however, is its ability to produce ABL and downburst winds at large scales simultaneously. Recently, Romanic et al. (2019) demonstrated this mode of the WindEEE Dome operation by analyzing the strength and momenta of nine different downburst-ABL combinations. Their work was focused on quantifying the strengths of two flows at their sources in the closed-circuit configuration of the WindEEE Dome simulator. Therefore, the near-surface interaction between downburst outflows and ABL winds was not addressed. The present study adopts one of the nine investigated configurations from Romanic et al. (2019) to investigate the near-surface downburst-ABL wind interaction.

The interplay between downbursts and ABL winds is similar to the classical fluid dynamics studies on the behavior of an impinging jet or a gravity current in a crossflow. Mahesh (2013) and Karagozian (2014) provide two recent reviews on this subject. The engineering research on impinging jets in crossflows showed that their interaction creates three distinct flow regions: (1) The potential core zone; (2) the zone of maximum deflection; and (3) the far-field zone. The potential core zone is the flow region that is closest to the nozzle, and the interaction between the flows is minimal (Kamotani and Greber, 1972). For instance, Romanic et al. (2019) investigated the potential core zone of downburst-like downdrafts in the WindEEE Dome. Strong pressure gradients across the jet and pronounced entrainment make the flow field inside the zone of maximum deflection most difficult to model analytically or numerically (Demuren, 1994). Regardless of jet and crossflow configurations, the dominant feature in this region of the flow is the shear that exists in the zone of maximum deflection and a couple of counter-rotating vortices that form in the jet and propagate downwards (Muppidi and Mahesh, 2005). Krothapalli et al. (1990) and Kelso and Smits (1995), among others, found the formation of horseshoe vortices upstream of the jet and their subsequent propagation downstream. The wake vortices behind the jet were reported in Wu et al. (1988) and Fric and Roshko (1994). Most of the above studies investigated the jets released into the crossflow without their impingement on the surface. Therefore, some of the above flow regions are difficult to identify in the case when the jet altered by crossflow hits the underlaying surface. In addition, most of the jets investigated in their work were steady, whereas downbursts are transient phenomena characterized by a sudden increase of wind speed, the velocity peak, and the subsequent decrease of velocity to the value of ABL winds that where present before the downburst event (Romanic et al., 2020a).

1.1. Experiments setup

The WindEEE Dome is a hexagonal wind simulator designed to reproduce downbursts, tornadoes, and ABL winds at a variety of geometric and velocity scales (Hangan et al., 2017). The test chamber is 25 m in diameter with the height and the side length of 3.8 m and 14.8 m, respectively. The isolated downburst mode, as well as the combined mode of downburst and ABL winds, are shown in Fig. 1. Isolated downbursts in the WindEEE Dome (Fig. 1a and b) are created by pressurizing the upper plenum using six large fans (2 m in diameter) and by closing the bell mouth louvers that connect the upper plenum and test chamber. When the pressure difference between the upper plenum and test chamber reaches a target value (~3.4 hPa), the bell mouth louvers are opened, thereby creating an impinging jet that is released into the test chamber. Various downdraft intensities and diameters in

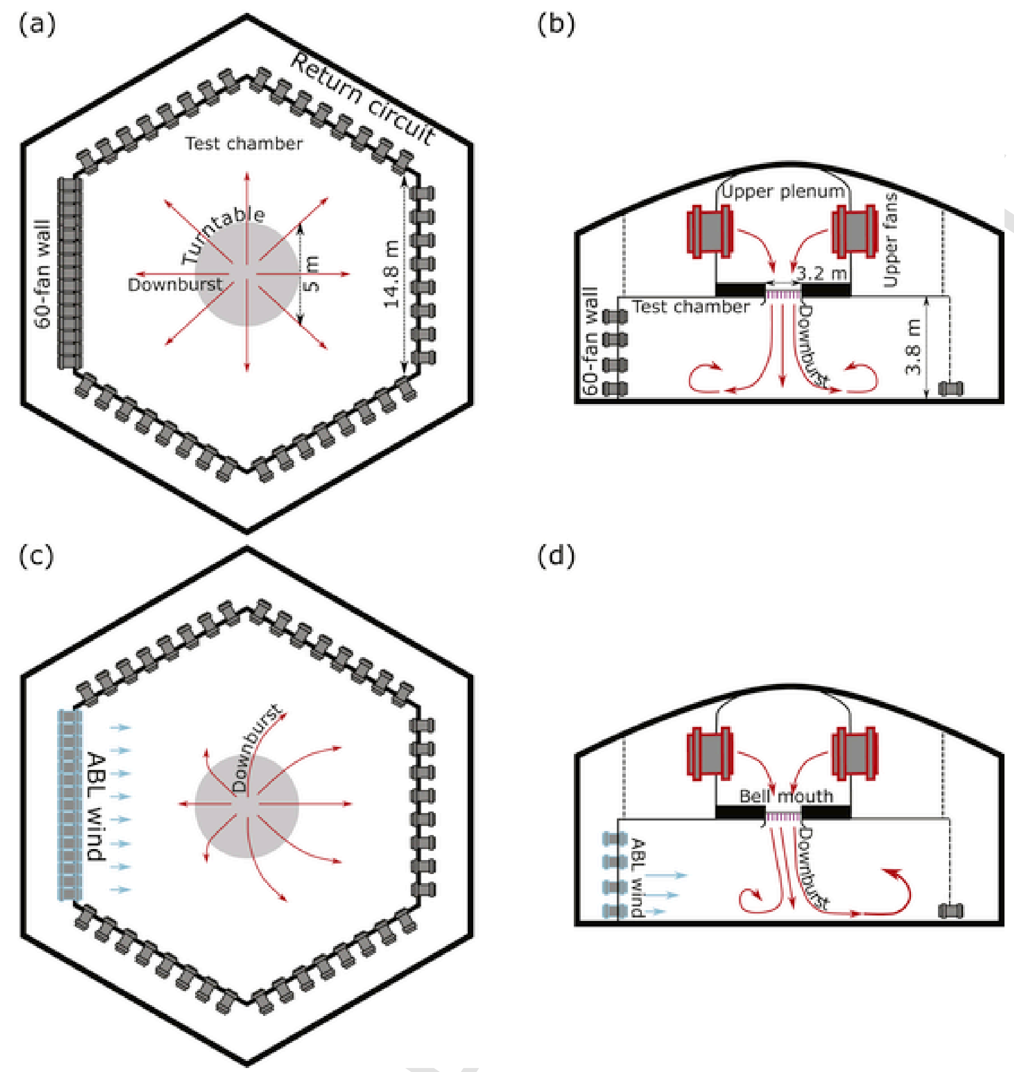

Fig. 1. (a,b) Isolated downburst and (c,d) downburst combined with ABL winds in the WindEEE Dome simulator. Downburst and ABL winds and their associate fans are depicted with red and cyan colors, respectively. The closed and opened positions of bell mouth louvers in (b) and (d) are indicated with grey and magenta colors, respectively. Schematics are not to scale. (For interpretation of the references to color in this figure legend, the reader is referred to the Web version of this article.)

the WindEEE Dome were investigated in Romanic et al. (2019), Junayed et al. (2019), Jubayer et al. (2019), and Romanic et al. (2020). Hereafter, the isolated downburst without ABL winds and the downburst combined with the ABL winds are abbreviated as DB and DBABL, respectively.

In the DBABL mode (Fig. 1c and d), the downdrafts in the WindEEE Dome are released into already developed ABL winds. The 60-fan wall was used to generate ABL winds with the bell mouth louvers being initially closed. Each of the 60 fans is 0.8 m in diameter, and the nominal power of each fan is 8.8 times smaller than the maximum power output of the six overhead fans (220 kW each). While the ABL winds were running in the testing chamber, the six fans situated in the upper plenum were used to build up the pressure difference between these two chambers. Then, similar to an isolated downburst, the bell mouth louvers were opened and the downdraft was released into the ABL winds. This mode of the WindEEE Dome is also described in detail in Romanic et al. (2019). While the generation of downdraft and ABL winds in the WindEEE Dome does not resemble the physical processes that trigger this interaction in the real atmosphere, the dynamics of combined DBABL outflow near the surface is similar to the real downburst outflows. The similarity will be demonstrated in this paper by comparing the DBABL results against field measurements and numerical simulations of this interaction.

The momentum ratio of downdraft to ABL winds used in this study is adopted from Romanic et al. (2019). In their work, downdraft momentum was calculated at the bell mouth exit, while the momentum of the crossflow was derived from ABL wind measurements close to the 60-fan wall. The six fans in the upper chamber were operated at 20% of their nominal revolution per minute (rpm), while the 60 fans in the testing chamber were set up at 30% of their nominal rpm. In this configuration, the mean center line jet velocity ($\bar{U}_{jet}$) at the bell mouth exit was 8.87 m s^{-1} in the DB case and 6.88 m s^{-1} in the DBABL experiment (Fig. 2). The asymmetry of the jet velocity profile at the bell mouth exit is observed in both DB and DBABL experiments, but it is larger in the latter case. The weakening of the DBABL downdraft in respect to the DB case is also observed in both along- and cross-ABL wind directions. These asymmetries in the DB downdraft might explain some of the asymmetries of the produced outflow that will be discussed later in Section 4. Romanic et al. (2019) further found that this configuration of the two flows—out of nine different configurations that they investigated—results in the largest downdraft weakening in comparison to the equivalent DB downdraft. The weakening of downdraft occurs due to the closed-circuit design of the simulator in which the inclu-

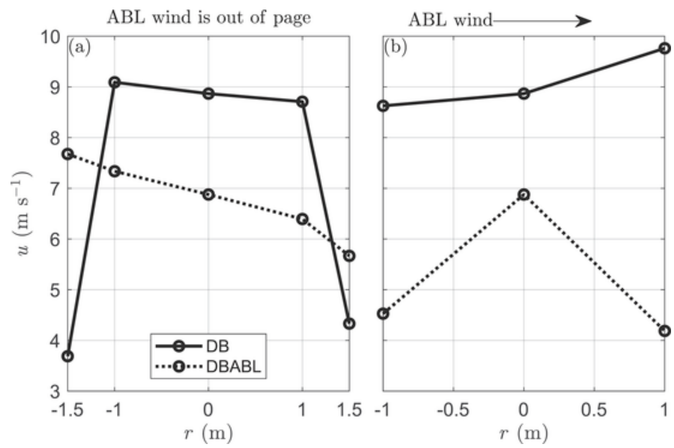

Fig. 2. Jet velocity profiles at the bell mouth exit extracted from Romanic et al. (2019) in the cross-ABL wind direction (a) and the along-ABL wind direction (b). The direction of the ABL winds in the DBABL case is indicated above each plot.

sion of ABL winds inevitably deteriorates the strength of downdrafts (Romanic et al., 2019). The investigated downdraft diameter in our study was $D = 3.2$ m (Romanic et al. 2019, 2020b; Junayed et al., 2019) (Fig. 1b). The other eight DB-to-ABL wind configurations from Romanic et al. (2019) will be investigated in future studies.

The ABL wind profile used in the DBABL experiments (Fig. 3) does not follow the standard Engineering Science Data Unit (ESDU) velocity profile for a specific type of terrain (ESDU, 2002). Thunderstorms usually occur in unstable or conditionally unstable atmosphere that does not follow the ESDU wind profiles for the neutral atmosphere expressed via:

$$u = 2.5u_* \left(\ln\left(\frac{z}{z_0}\right) + 34.5\frac{fz}{u_*} \right) \quad (1)$$

Here, u_* is the friction velocity, z_0 is the roughness height, $f = 2\Omega \sin\phi$ is the Coriolis parameter, and Ω and ϕ are the Earth's angular velocity and latitude, respectively. By assuming $\phi = 39°$N

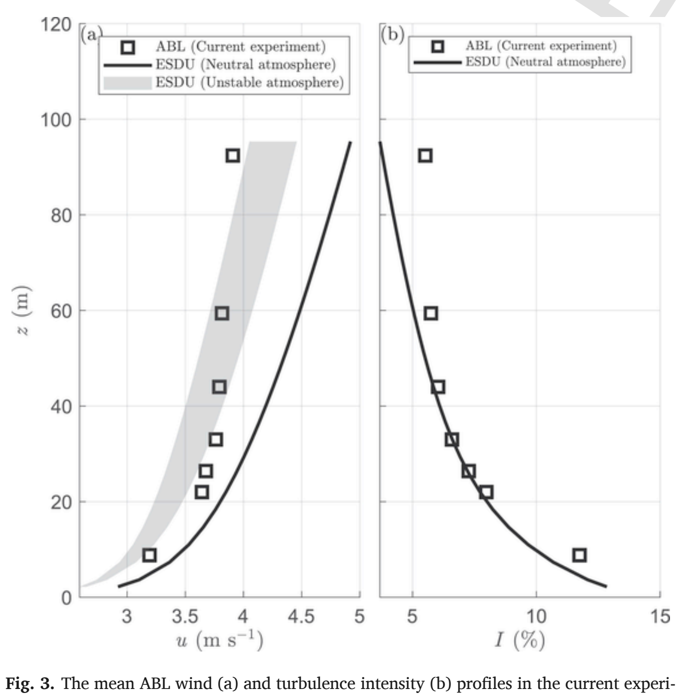

Fig. 3. The mean ABL wind (a) and turbulence intensity (b) profiles in the current experiment (squares) and the ESDU standard for the thermally neutral (black line) and unstable atmosphere (grey shaded region). The profiles are measured at the turntable center.

to match the field campaign from Hjelmfelt (1988), $u_* = 0.134$ m s^{-1} and $z_0 = 0.0004$ m were estimated by fitting the log-law wind profile to the measured ABL wind profile in the WindEEE Dome (Fig. 2a). Here, the geometric scale of ABL is taken to be the same as the mean geometric scale of downbursts in the WindEEE Dome (1:220) (Romanic et al., 2020b). Fig. 2a shows that the ESDU profile for neutral atmosphere does not match the wind tunnel measurements.

To account for atmospheric stability, Eq. (1) is altered by adding the stability term via:

$$u = 2.5u_* \left(\ln\left(\frac{z}{z_0}\right) + 34.5\frac{fz}{u_*} - \Psi\left(\frac{z}{L}\right) \right). \quad (1)$$

where $\Psi(z/L)$ is the stability term derived from the Monin-Obukhov similarity theory and L is the Obukhov length. The stability function for unstable atmosphere was taken from Businger et al. (1971) and Nieuwstadt (1978) as:

$$\Psi\left(\frac{z}{L}\right) = 2\ln\left(\frac{1+s}{2}\right) + \ln\left(\frac{1+s^2}{2}\right) - \arctan(s) + \frac{\pi}{2}, \quad (2)$$

where

$$s = \left(1 - 15\frac{z}{L}\right)^{\frac{1}{4}}. \quad (3)$$

Markowski et al. (2019) reported that the range of L values during thunderstorm days, but before the arrival of the cold outflow is in the range between −50 and −500 (mean around −200). Using this interval of L, Fig. 2a shows that the mechanically generated ABL wind profile in the WindEEE Dome resembles more closely the unstable atmosphere than the neutral stratification. The emphasis here is on the phrase "mechanically generated ABL wind profile" because the WindEEE Dome chamber is isothermal and the shape of the profile is governed by rpm configuration of 60 fans.

Because the profile is mechanically created, the turbulence properties are not necessarily following the turbulence in an unstable atmosphere (Fig. 2b). Instead, the turbulence intensity (I) profile in the present experiments follows the ESDU standard for the neutral atmosphere up to the height of approximately 60 m above the ground. The matching of ESDU turbulence is probably due to the isothermal properties of the chamber and the fact that the mean profile is mechanically created using a system of fans, rather than through a combination of mean flow shear and mixing due to heat fluxes (thermal effects) that exist in a stratified atmosphere.

All velocity measurements in this research were performed using four-hole Cobra probes developed by the Turbulent Flow Instrumentation Pty. Inc. Their output sampling frequency was set at 2500 Hz, and the sampling time was 120 s. Guo and Wood (2001) compared Cobra probes against hot-wire anemometers and demonstrated their capability to measure mean velocities and fluctuations in highly turbulent flows reliably. The Cobras were designed to measure the incoming flow within a cone of 45°, but the uncertainty of measurements increases as the inflow angle approaches 45°.

The Cobra probes setup is portrayed in Fig. 4. In total, six probes were used for downburst outflow measurements, while one Cobra probe was employed for ABL wind measurements. The ABL probe (cyan probe in Fig. 4) was always located at the same non-dimensional radial distance (r/D; r is the radial distance in polar coordinates) and azimuth angle (θ) as the rake with downburst Cobra probes (red probes), but the ABL wind probe was positioned on the opposite side of the symmetry line concerning the incoming direction of ABL winds (see Fig. 4a). This setup enabled the simultaneous measurements of downburst outflow and the streamwise ABL wind component at the same lo-

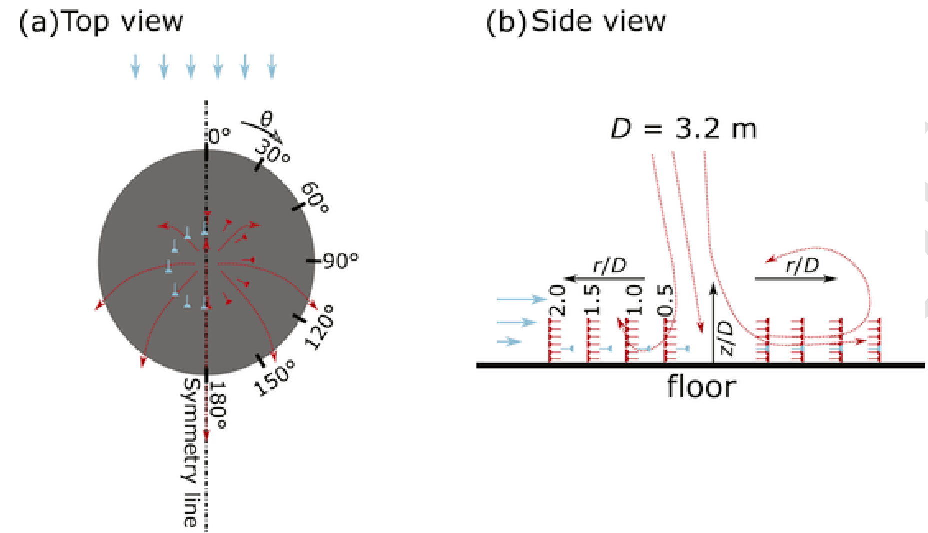

Fig. 4. Top (a) and side (b) views of the experiment setup. The red Cobra probes were always pointing to the center of the turntable, and they were used to measure the radially outward component of downburst outflow. The cyan Cobra probe was always oriented towards the direction of ABL winds. (For interpretation of the references to color in this figure legend, the reader is referred to the Web version of this article.)

cation, assuming the above-invoked flow symmetry. For $\theta = 0°$ and 180° , the ABL probe was in the opposite and the same direction as the downburst probes, respectively. For $\theta = 90°$, the two sets of probes were perpendicular. The heights of the downburst probes were 4, 10, 15, 20, 27 and 42 cm above the floor, while the ABL probe was positioned at 13 cm above the floor. The investigated azimuth angles in respect to the incoming ABL winds were from 0° to 180° with an angle increment of 30° (Fig. 4a). Four different radial distances (r/D) from the isolated downdraft center were considered: 0.5, 1.0, 1.5 and 2.0, as well as one additional set of measurements performed in the center of isolated downdraft impingement, i.e., $r/D = 0.0$. Here, the r/D distances are measured from the center line of the DB downdraft and the potential deflection of the DBABL downdraft is not accounted for in the present analysis. Since the Cobra probe measurements are not suitable for an estimation of downdraft deflections from the vertical jet, all radial distances are referenced to the isolated DB case. This referencing to DB case introduces a level of uncertainty of the reported r/D values in the DBABL outflow.

The percentage of valid DB velocity readings (velocity threshold at 2 m s^{-1}) at different r/Ds and θs was very high (Table 1). In the DBABL case, however, the percentage of valid data is highly dependent on both r/D and θ. No valid data were recorded by the DB Cobra probes for $r/D > 1$ and $\theta \leq 30°$ due to their orientation into the DBABL outflow propagation (Fig. 4). The measurements were conducted for a given r/D and θ location and then the Cobra probe masts were moved to another location. All experiments were repeated four times to assess the uncertainty and variability of the obtained results. Throughout this paper, $\left(\overline{\blacksquare}\right)$ and $\left(\widetilde{\blacksquare}\right)$ stand for the time averages and ensemble means of ($\blacksquare$), respectively, whereas $\left(\widehat{\blacksquare}\right)$ is used for peak values.

Table 1
Percentage of accurate velocity readings at different radial locations r/D (rows) and different azimuths θ (columns). The values outside and inside the brackets correspond to DB and DBABL cases, respectively. The reported figures are for all heights because the percentages difference of valid data between different heights was < 1% (not shown). The velocity threshold for the Cobra probes was set at 2 m s^{-1}.

	0°	30°	60°	90°	120°	150°	180°
0.5	100 (98)	99 (92)	99 (86)	100 (81)	99 (88)	100 (99)	100 (100)
1.0	99 (76)	97 (88)	97 (95)	99 (98)	98 (99)	100 (100)	100 (100)
1.5	92 (0)	88 (0)	90 (74)	93 (93)	89 (99)	95 (99)	97 (99)
2.0	92 (0)	87 (0)	88 (2)	89 (83)	89 (98)	89 (96)	93 (95)

2. Downburst records segmentation

While the velocity sampling time was 120 s, transient segments of the DB and DBABL outflows in the present experiments are in the order of seconds and below (Fig. 5a). Therefore, a procedure was developed to systematically and objectively extract the transient segments from the entire time series of the radial velocities (u). Instead of terminating downdrafts after a few seconds and only generate the transient portion of the signal, the sampling time was set at 120 s to model both the transient and stationary states of the outflows. The separation between transient and stationary segments was performed objectively due in no small number of tested cases and the removal of possible subjective biases. The methodology to isolate transient segments from the rest of the time series is as follows.

(1) A moving mean filter, $\bar{u}(t)$, with the averaging window of 0.05 s (Junayed et al., 2019; Romanic et al., 2020b), is applied to the instantaneous velocity (Fig. 5a) for the removal of the highest-frequency fluctuations (Fig. 5b).
(2) If $\theta > 90°$:
a. A changepoint detection method (Lavielle, 2005; Killick et al., 2012) is applied to the smoothed velocity record as proposed by Romanic et al. (2019, 2020a) (Fig. 5b). In this step, the method seeks to determine two changepoints (k_1, k_2) that isolate downburst segments from the entire velocity record. This segment is enclosed by the two dash-dotted lines in Fig. 5b.

2.1. Otherwise (i.e., $\theta \leq 90°$)

b. The changepoint method is not required due to the absence of ABL winds in the velocity records from the downburst Cobra probes that are pointing into the DBABL outflow propagation (see Fig. 4). In this case, the first valid velocity reading and the end of the record are used instead of k_1 and k_2.

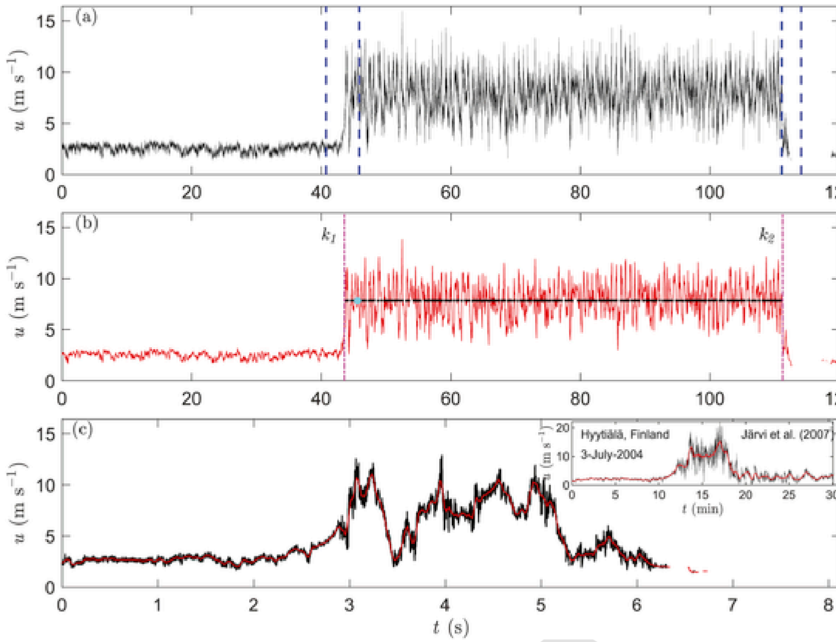

Fig. 5. DBABL velocity measurements at $\theta = 150°$, $r/D = 1.5$, $z = 15$ cm. (a) Instantaneous velocity (black line) with the transient segments included between the dashed (blue) lines. (b) Moving mean (red line) of the instantaneous data together with the locations of two changepoints (k_1, k_2; the magenta dash-dotted lines). The black and cyan ($I_p = 7$) dots show the intersection points between the mean velocity in the $[k_1, k_2]$ interval and the moving mean record (see text for details). (c) The extracted DBABL velocity record (black; instantaneous velocity), the associated moving mean record (red) and real downburst velocity record from Finland (Järvi et al., 2007). The DBABL velocity record in (c) is the merge of two transient segments in (a). (For interpretation of the references to color in this figure legend, the reader is referred to the Web version of this article.)

(3) Then, find the intersection points between the mean, $\bar{u}$, of the isolated segment in Step (2) and the smoothed velocity record in Step (1). The obtained intersections are shown as black dots, including the highlighted cyan dot, in Fig. 5b.
(4) The seventh intersection point ($I_p = 7$; the cyan dot in Fig. 5b) is selected as the end of the initial transient part of velocity signals. This portion of the record contains velocity ramp-up, first velocity peak, and velocity slowdown after the peak. The choice of $I_p = 7$ is empirical and based on numerous sensitivity tests. However, since the crossing frequency of $\bar{u}$ and $\bar{u}(t)$ (t is the time) is high due to the high sampling frequency of the Cobra probes, a change of $I_p \pm 3$ does not significantly influence the lengths of isolated segments.
(5) The velocity segments between $I_p = 7$ and the second changepoint (if $\theta > 90°$) or the end of the record (if $\theta \leq 90°$) are deemed as stationary.

The effectiveness of this methodology at extracting downburst-like segments from the instantaneous velocity data is demonstrated in Figs. 5 and 6 for two different locations in the outflow. The isolated DBABL segments are shown in Figs. 5c and 6c together with two anemometer records of real downbursts from Finland (Järvi et al., 2007) and Italy (Romanic et al., 2020b). The two real events are included for qualitative comparison against the experimental data. The proposed methodology provides flexibility on isolating DB-like portions of different lengths from the entire velocity record. This tuning can be archived by changing the reference intersection point, $I_p = 7$, to another value, as well as by changing the length of the moving average window. This method provides an objective separation of the initial peak in the experimentally produced downburst records from the rest of the steady-state time series.

All DBABL records are segmented into ABL winds, transient and steady-state segments, and the velocity dissipation portions (Fig. 7a). This study is mainly concerned with the transient and stationary segments. The transient part, in turn, can further be subdivided into the ramp-up, the peak, and the ramp-down segments in most cases (Fig. 7b). A single dominant peak and the ramp-down segments were not always observed in the DBABL winds (Fig. 5) depending on the location in the outflow. The initial transient segment in velocity records characterize the passage of the first (primary) vortex in the DB-like outflows. The stationary segments are the product of a continuous and steady-state impingement of the downdraft onto the surface that is established after the initial, transient stage. The similar DBABL records are not observed in physical experiments without ABL winds (e.g., Letchford et al., 2002; Hangan et al., 2019; Junayed et al., 2019; Romanic et al., 2020b). Visually, the isolated DBABL segments in Figs. 5 and 7 nicely resemble some of the observed downbursts in nature (De Gaetano et al., 2014; Burlando et al., 2017; Romanic et al., 2020a). This similarity is also shown in Figs. 5 and 6 in the qualitative comparison between the extracted DBABL records and the real events from Europe. While both full-scale events are transient, the peak duration and ramp-up are different between the two records. The similar observations can be made for the two DBABL velocity records that are acquired in different parts of the outflow. However, the similar transient signatures are observed in both sets of velocity records. Moreover, Fig. 5 shows that the ratio of the mean peak velocity in the transient portion of the records to the mean ABL wind speed before the downburst is similar between the Finland downburst and DBABL record from the current experiments. The mean peak velocities in downbursts are typically 2–4 times higher than the mean wind ABL wind speed before the event (Romanic et al., 2020a).

Another feature worth discussing here is the pattern observed in dissipation segments of DBABL records. Depending on the location in the outflow, the return to ABL winds after the termination of the downdraft is not immediate. Instead, the wind speeds first deteriorate below the mean velocity of ABL winds before reaching the intensity of the ABL winds that was observed prior to the downburst (Fig. 7). This feature is often observed in real downburst outflows (Burlando et al., 2017), and it is likely associated with remnants of the downburst degrading the ABL winds in the dissipation stages of thunderstorm outflows (Wakimoto, 1982). Once the downburst-related flow struc-

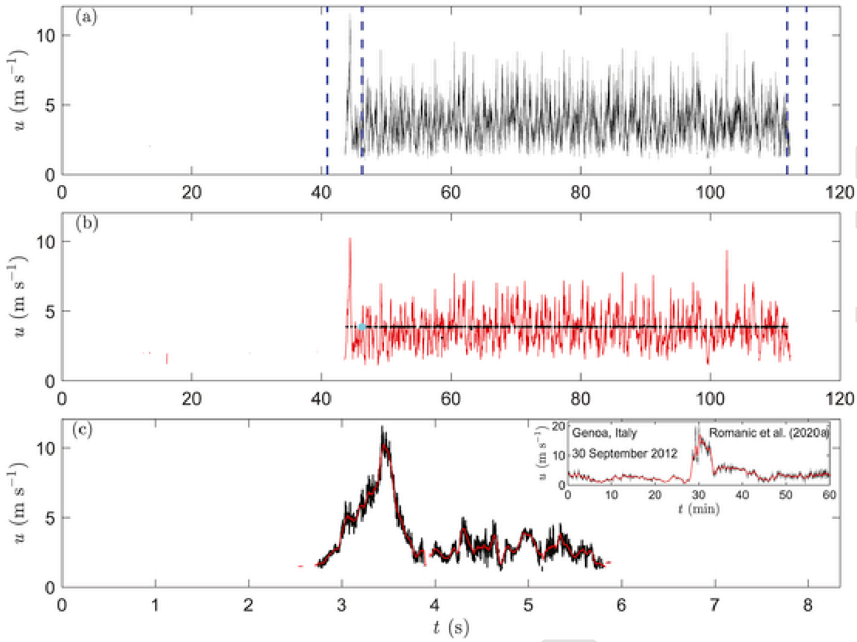

Fig. 6. DBABL velocity measurement at $\theta = 60°$, $r/D = 0.5$, $z = 27$ cm. The ABL wind prior to the downdraft release is not observed in the record due to the orientation of the downburst Cobra probes at $\theta = 60°$ (see Fig. 4). Interpretation of different lines and symbols as in Fig. 5. In (c), the embedded figure in the top-right shows a real downburst from Italy (Romanic et al., 2020b).

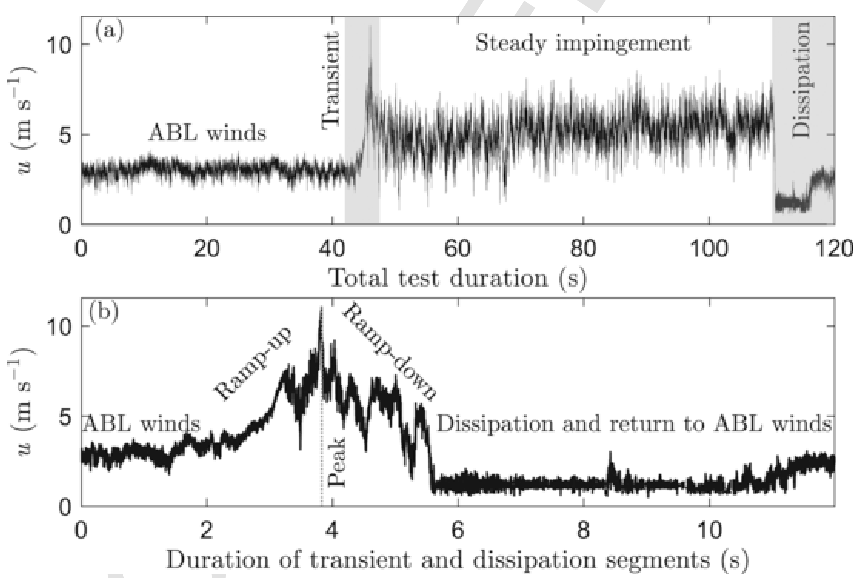

Fig. 7. Identification of different segments in DBABL outflows achieved using the proposed segmentation methodology. The transient and dissipation (shaded) regions in (a) are shown in (b). The time axis in both subplots is relative to the length of the record and always starts from zero. The dotted line in (b) shows the location of the primary velocity peak. The velocity records correspond to $\theta = 180°$, $r/D = 0.5$ and z= 10 cm.

tures entirely dissipate due to the absence of their forcing from the parent cloud (i.e., the downdraft is extinguished), the flow field returns to the ABL winds. This feature of velocity records is not observed in the physical simulations of downbursts that do not account for the existence of ABL winds.

3. Results

3.1. Peak and mean velocity profiles

Vertical profiles of enveloped peaks of radial velocity component (u) are different in the DB and DBABL outflows (Fig. 8). The shown profiles are an ensemble average of four experiment repetitions. All peaks in this study are the maximum values in moving-mean velocity records obtained using a 0.3-s averaging window (Romanic et al., 2020b). Depending on the size and intensity of full-scale downbursts, the geometric scales of the WindEEE Dome downbursts are in the range between 1:100 to over 1:500 (mean geometric scale is 1:220). The velocity scales are usually around 1:2 to 1:3. Scaling of the WindEEE Dome downbursts to full-scale events is discussed comprehensively in Romanic et al. (2020).

The differences between the enveloped peak profiles in DB and DBABL winds (Fig. 8) depend on location in the outflow because of the asymmetric nature of the DBABL flow field. The enveloped peaks in the two outflows are similar at the lowest few heights at $\theta = 90°$ and 180° (Fig. 8b and c), but the spread between the profiles increases with height. At $\theta = 0°$—when the DBABL outflow is propagating against

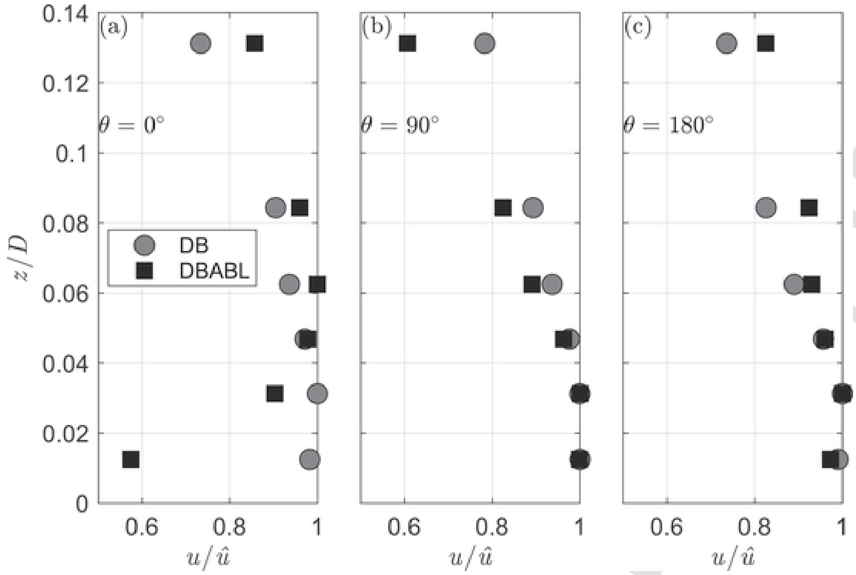

Fig. 8. Enveloped peak radial velocity profiles in the transient segment (primary vortex) of the DB and DBABL outflows at three different azimuth locations (a to c) and $r/D = 1.0$. Velocity is normalized to the maximum value, and the height is normalized to downdraft diameter.

ABL winds (Fig. 4)—the DB and DBABL profiles significantly differ from each other at all heights (Fig. 8b and c). The nose-like curvature in the DBABL enveloped peak profile is the most pronounced at $\theta = 0°$ and $r/D = 1.0$. The complexity of the DBABL outflow in this region is much higher than for $\theta \geq 90°$ where the downburst outflow propagates in the same direction as the ABL winds. The DB-ABL wind interaction hinders the full development of the primary vortex in the DBABL outflow at $\theta = 180°$ (Mason et al., 2010). The vortex modifications in DBABL outflow in comparison to an isolated DB are different from one location in the outflow to another due to different wind directions of DB outflow and ABL winds.

The mean velocity profiles in the steady-state segments of the two outflows (Fig. 9) resemble similar trends to those observed in the enveloped velocity peaks in Fig. 8. The smallest discrepancies between the two profiles are observed when the outflow is propagating perpendicular to the ABL winds ($\theta = 90°$).In this case, the maximum velocity is observed at the lowest elevation, and the spread between the profiles is constant throughout the height. The nose-like curvature in the DBABL profile at $\theta = 0°$is pronounced to the extent that the entire profile is symmetric around $z/D = 0.0625$ ($D = 3.2$ m is the downdraft diameter). A few of the analyzed profiles (e.g., Fig. 9b) indicate that velocity measurements below 4 cm ($z/D = 0.0125$) are needed to properly characterize the flow region closest to the surface.

It is worth mentioning that in an ideal downburst simulator, the DB profiles measured without ABL winds (i.e., isolated downburst) should be independent of θ due to the circular symmetry of the outflow (Fig. 1). However, slight dependency on θ is observed in the present experiments. These imperfections are due to the observed asymmetry of the downdraft at its source (Fig. 2) and due to boundary conditions in the testing chamber (e.g., existence to the sidewalls in the chamber and possible floor irregularities). With the large sizes of downdrafts ($D = 3.2$ m), the testing chamber of 25 m in diameter and chamber ceiling height (H) of 3.8 m in height, it is extremely challenging to entirely remove all potential factors that can slightly contaminate

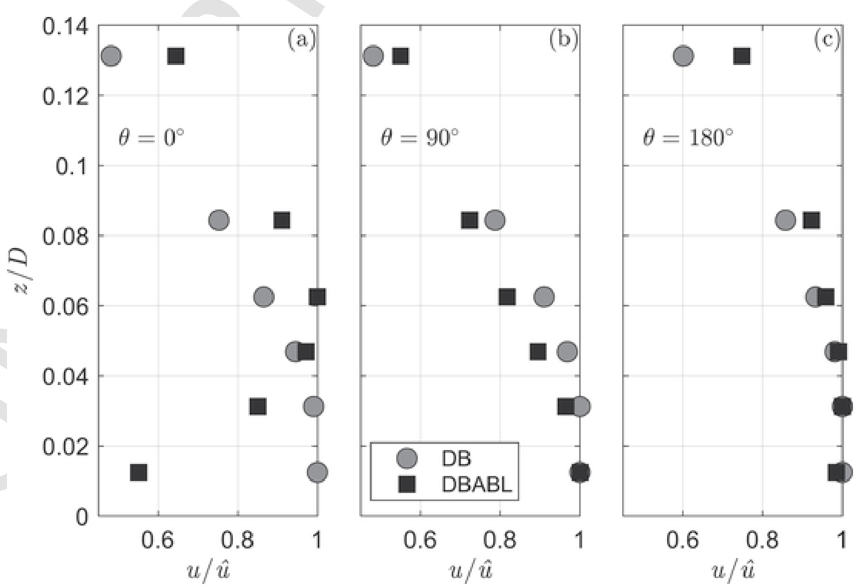

Fig. 9. Mean radial velocity profiles in the steady segment of the DB and DBABL outflows at three different azimuth locations (a to c) and $r/D = 1.0$.

the flow field. The dependency of the DB flow field on H/D in the WindEEE Dome was recently discussed in Junayed et al. (2019). The velocity profiles from the downdrafts with $H/D>1$—such are the ones in this study—have stronger nose-shape curvature and better resemblance of full-scale downbursts than the outflows with $H/D<1$. The influence of boundary conditions on DB velocity profiles was also addressed in Xu and Hangan (2008). Also, the downdrafts in the WindEEE Dome are created by utilizing six powerful fans in the upper chamber (Fig. 1) and a small rpm difference between the fans, as well as any geometric imperfection of the blades, can result in the skew of the downdraft that was observed in Fig. 2. This asymmetry can further cause the observed differences in peak and mean velocity profiles in the near-surface regions of the DB outflows. The presence of louvers inside the bell mouth can additionally influence the symmetry of downdrafts. Thus, the velocity profiles across the impinging jet in Fig. 1 are measured downstream from the louvers (Romanic et al., 2019) in order to assess the final level of asymmetry of the downdrafts before their impingement onto the floor. Later in Section 4.2, the study further demonstrates the high fidelity of isolated DB outflows in the WindEEE Dome chamber.

The produced DBABL outflow corroborates well with the numerical simulations of tilted downdraft in Mason et al. (2010) (Fig. 10). Two ratios between the ABL winds and the strength of the negatively buoyant downdraft ($u_{ABL,ref}/U_{jet,ref}$) in Mason et al. (2010) were E21 = 0.21 and E37 = 0.37. In their work a wind speed at 2 km above the surface was used as an estimate for the ABL wind strength ($u_{ABL,ref}$), whereas $U_{jet,ref}$ was estimated as the downdraft velocity in the absence of the ABL winds. The same approach applied to the DBABL case in our study yields the ratio of E44 = 0.44, which is reasonably close to E37 in Mason et al. (2010). However, it should be noted that our ABL wind measurements were conducted at a much lower elevation than 2 km (full-scale equivalent). Regardless of these differences, there is a definite similarity between their Computational Fluid Dynamics (CFD) results for the E37 case and the current physical experiments (E44) at $\theta = 180°$ and $r/D = 1.5$ (Fig. 10). The matching is higher for the enveloped peaks than instantaneous profiles. The uncertainty of peak values due to turbulent fluctuations that is found from four experiment repetitions, however, demonstrates an advantage of physical experiments over numerical simulations in this respect. The physical experiments show that the spread around the ensemble mean from the four repetitions increases with the height throughout the flow. The higher elevations in the outflow are in the strong shear region characterized by Kelvin-Helmholtz instability (Charba, 1974; Kim and Hangan, 2007) that amplifies turbulence, thus producing more variable peaks between different test repetitions. This natural variability is not present in the Unsteady Reynolds Averaged Navier-Stokes (URANS) simulations that only resolve large-scale features in the flows (Kim and Hangan, 2007; Mason et al., 2010; Skote et al., 2018) However, the similarity between the physical experiments and the URANS is high (Kim and Hangan, 2007; Mason et al., 2010) in terms of the general features observed in the moving-mean of transient flows.

The present physical experiments fall within the envelope of observed peak velocity profiles from the JAWS field study (Hjelmfelt, 1988) (Figs. 10 and 11). Due to the slow scanning periods and other limitations of Doppler radars deployed in the JAWS campaign, the obtain profiles cannot be considered as either instantaneous or the real enveloped peaks, but they are likely a closer resemblance of enveloped peak values (Mason et al., 2010). The downburst diameters in the JAWS data from Hjelmfelt (1988) are between 1.2 and 3.1 km with the mean diameter of 1.8 km. On average, the JAWS downdrafts are about 550 times the WindEEE Dome downdraft used in this study (3.2 m). The maximum velocities in the JAWS data are up to two times higher than the peak velocities in the present DB-like experiments. This range of geometric and velocity scales is in the interval of established WindEEE Dome downburst scales in Romanic et al. (2020b).

A large portion of the enveloped peak velocity profiles from the current experiments also falls outside of the JAWS region (Fig. 10). The nose-shaped velocity profile that is usually associated with downburst winds is, in fact, not always observed in real thunderstorm outflows (Choi, 2004; Gunter and Schroeder, 2015). The DBABL experiments show that the nose-like curvature reduces with moving away from the downdraft center, as the outflow diminishes and the flow field approaches the state of surrounding ABL winds. However, there is also a strong dependency of velocity profile's curvature on θ. The nose-like curvature in the DBABL outflow is the most pronounced at $\theta = 0°$ and the least pronounced at $\theta = 180°$.

In the region around $\theta = 0°$, the DBABL outflow caused by the inclined downdraft is propagating into the oppositely blowing ABL winds. The downdraft inclination that is towards $\theta = 180°$ elongates the primary vortex that is in the forward region of the outflow in the direction of ABL winds (i.e., towards $\theta = 180°$; forward region) (Mason et al., 2010), and contracts the vortex that is in the rear part of the outflow in the streamwise direction (i.e., rear region). That is, the interaction between the ABL winds and the downburst outflow in the rear and forward regions of the outflow is profoundly different. This interaction is observed in three different ways in the present experiments, as described below.

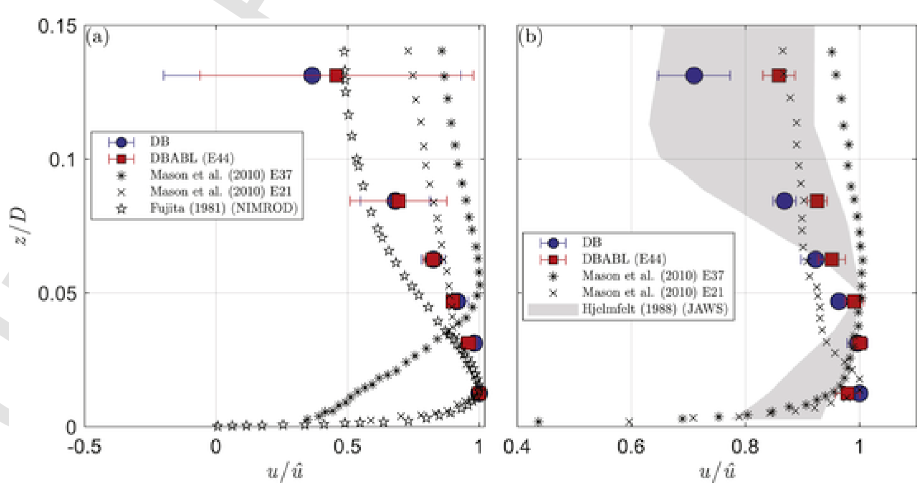

Fig. 10. (a) Instantaneous maximum and (b) enveloped peak velocity profiles during the transient portion of velocity records and their comparison against literature. See text for the interpretation of E44, E37, and E21. The error bars show one standard deviation of the obtained values from four experiment repetitions.

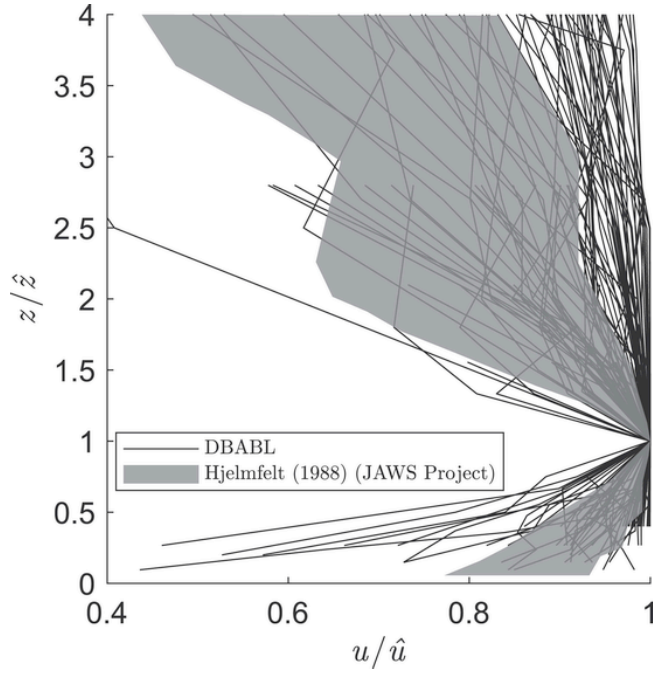

Fig. 11. Comparison of all enveloped peak profiles in the DBABL outflow during the transient portion of velocity records against the full-scale data from the JAWS project. As in Hjelmfelt (1988), the height is normalized to the height of the maximum velocity.

The more pronounced nose-like curvature in the rear region indicates a strong vertical shear in the outflow (Figs. 8 and 9). Because of the weak shear in the ABL winds above approximately $z/D = 0.046$ (Fig. 3), the opposite vorticity in the ABL winds at these heights does not entirely deteriorate the vortex. Instead, the return flow in the upper regions of the vortex is likely intensified by the ABL winds (Fig. 12). These high winds are brought down to near the surface and back into the vortex due to the circulation pattern in the rear outflow (Fig. 12). Indeed, around $r/D = 0.5$ and $\theta = 0°$, the DBABL outflow is stronger than the DB winds. On the other side, the ABL winds that are passing around the downdraft in our experiments gain the downward momentum that hinders the full development of primary vortex in the forward region (Mason et al., 2010).

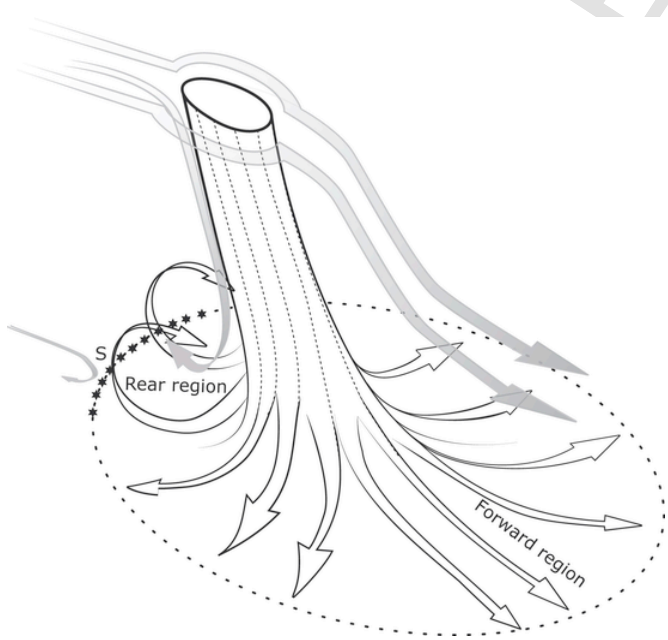

Fig. 12. Conceptual model of the DBABL outflow. The symbol "S" in the rear region indicates the stagnation point in the flow due to the opposite vorticity in the DBABL outflow and ABL winds. The frontal line made of the star symbols in the rear region indicates the maximum radial distance to which the primary vortex can advance.

Secondly, the vortex in the rear side of the downdraft is at a higher elevation than in the isolated DB case (Orf and Anderson, 1999; Barata and Durão, 2004), which further contributes to the development of the strong nose-like curvature in the DBABL profiles at $\theta = 0°$ (Figs. 8 and 9). The higher elevation of the rear DBABL primary vortex in respect to the DB case is caused by the oblique downdraft impingement and the opposite vorticity of the ABL winds and the primary vortex close to the surface (Fig. 12). The opposite vorticity between the near-surface ABL winds and DBABL outflow at $\theta = 0°$ creates a stagnation region close to the surface that acts to elevate the radially propagating primary vortex. Fig. 8 demonstrates that the maximum velocity in the primary vortex of DBABL outflow is observed at higher elevations than in the DB case.

Thirdly, the ABL winds prevent radial propagation of the rear primary vortex beyond approximately $r/D = 1.0$ at $\theta = 0°$. Similar findings were also reported by Barata and Durão (2004), who demonstrated that the radial distance to which the vortex propagates depends on the strength of downdraft and crossflow. The numerical simulations of Orf and Anderson (1999) also corroborate well with their finding and the pressent results of DBABL experiments. The current experiments further demonstrate this observation in the following section that shows high DBABL velocities at $r/D = 0.5$ and $\theta = 0°$, but, at the same time, the complete absence of the DBABL outflow for $r/D > 1$ (at $\theta = 0°$). Therefore, the vortex never propagated beyond around $r/D = 1.0$. Moreover, the velocity records at $r/D = 1.0$ lack a single, dominant, and transient peak (Fig. 13), which also indicates that the vortex never traversed that measurement point. Instead, the velocity records are made out of a series of intermittent peaks of different magnitudes that indicate highly turbulent flow that is characterized with profoundly different dynamics than the flow field in the forward region of the outflow (Fig. 5). The larger standard deviation of enveloped peaks obtained from multiple experiment repetitions in the rear side of the outflow (for $\theta \leq 60°$) also demonstrates the high complexity of the outflow in this region.

We further benchmark our results against two thunderstorm wind measurements from the United States (US; Gunter and Schroeder, 2015) (Fig. 14) and a field campaign from Australia (Sherman, 1987) (Fig. 15). In both cases, the DBABL enveloped peak profiles follow the field measurements better than in the case of instantaneous profiles of maximum velocity. This analysis suggests that the

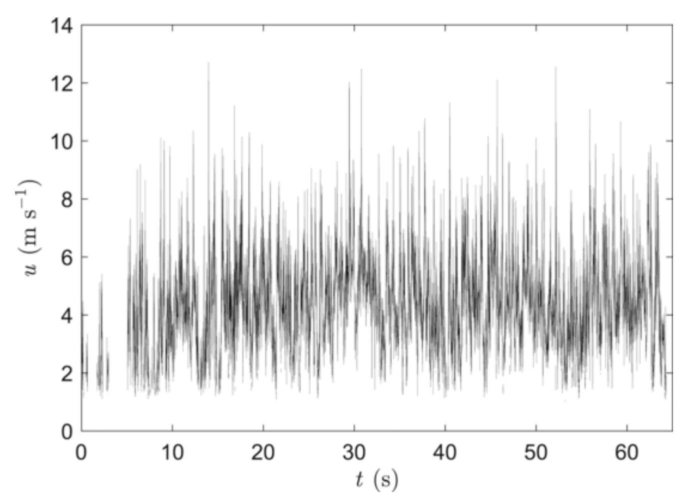

Fig. 13. Instantaneous radial velocity record in the DBABL outflow at $\theta = 0°$ and $r/D = 1.0$
.

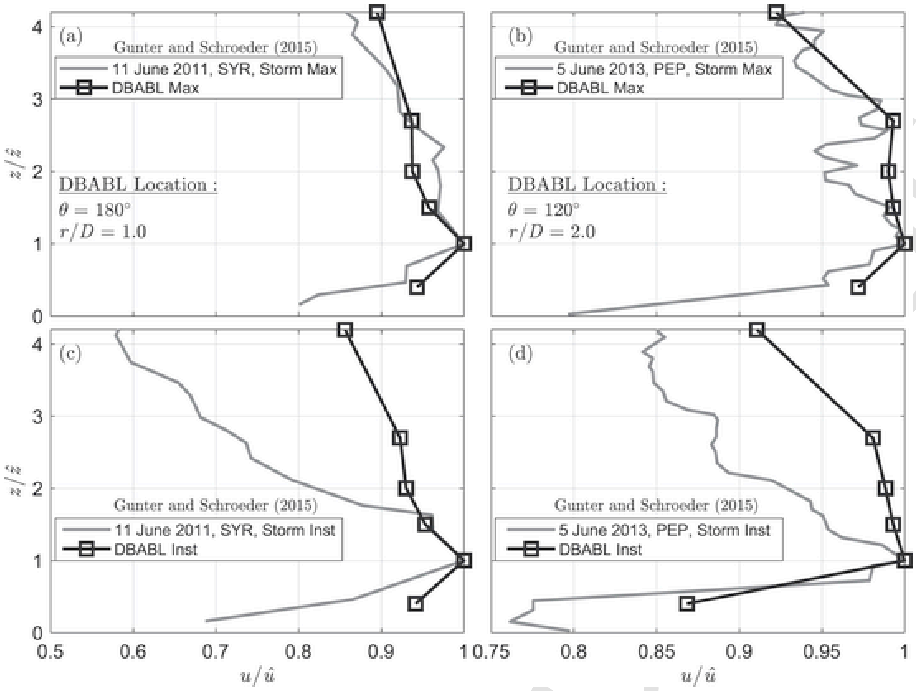

Fig. 14. The enveloped peaks (a, b) and the instantaneous maximum velocity profiles (c, d) in the Syracuse (a, c) and Pep (b, d) thunderstorm events (in the US) from Gunter and Schroeder (2015) and in the present DBABL tests. The maximum instantaneous velocity profile is extracted at the instant of the enveloped peak velocity at $z/\hat{z} = 1$ during the transient portion of velocity records.

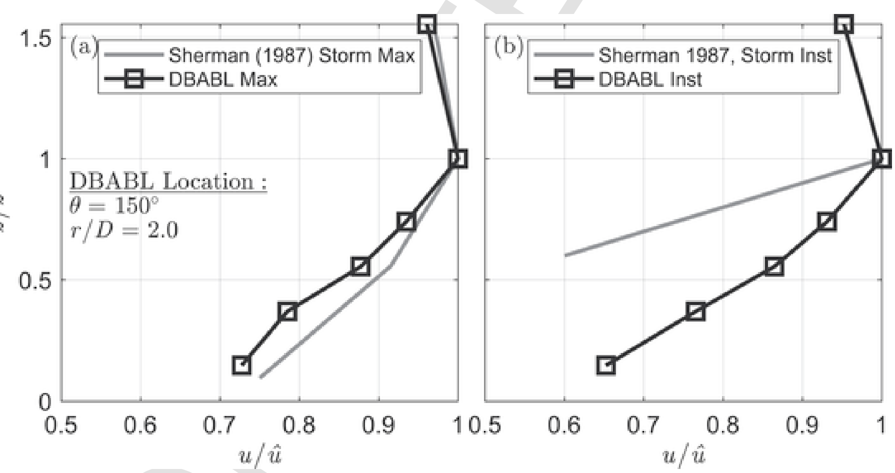

Fig. 15. The enveloped peaks (a) and the instantaneous maximum velocity profiles (b) in downburst close to Brisbane (Australia) from (Sherman, 1987) and in the present DBABL tests. The maximum instantaneous velocity profile is extracted at the instant of the enveloped peak velocity at $z/\hat{z} = 1$during the transient portion of velocity records.

DBABL simulations can be used as a tool to estimate the overall velocity peaks in downburst outflows, but not necessarily the instantaneous velocity profiles. However, since the current DBABL experiments were not conducted with the goal to match any particular case study of a full-scale downburst, the better matching of instantaneous profiles would likely be observed if that was the main goal of this research.

The present results also demonstrate that multiple repetitions of experiments provide an assessment of the uncertainty of obtained velocity peaks (Fig. 10). The enveloped peaks are more relevant than the instantaneous velocity profiles for wind engineering applications and downburst wind loading codification. In this context, the current DBABL experiments have shown that the enveloped peaks are better simulated than the instantaneous velocity profiles. The overestimation of velocity peaks close to the surface in the physical experiments (Fig. 14) is probably due to the experiments being conducted over a bare floor that resembles the low surface roughness (Section 2). Lastly, multicellular thunderstorms analyzed in Gunter and Schroeder (2015) and Sherman (1987) represent the most common type of thunderstorm systems in mid-latitudes (Markowski and Richardson, 2010, p. 209), which additionally highlights the importance of the good agreement of enveloped peaks profiles in DBABL experiments and full-scale data in Figs. 14 and 15.

The evolution of DB and DBABL radial velocity profiles throughout the transient segment (i.e., the primary vortex passage) of the velocity records at $\theta = 180°$ and $r/D = 1.5$ is plotted in Fig. 16. The profiles evolve similarly around the time of peak velocity, but the DBABL profile is characterized by a less pronounced nose-shaped curvature. During the initial stages of the ramp-up, the DB profile does not resemble the typical nose-like curvature that is usually associated with downburst winds. This evolution of DB profiles corroborates with the results in Junayed et al. (2019) that showed the absence of the nose-like curvature in the DB outflows during the ramp-up portion of the veloc-

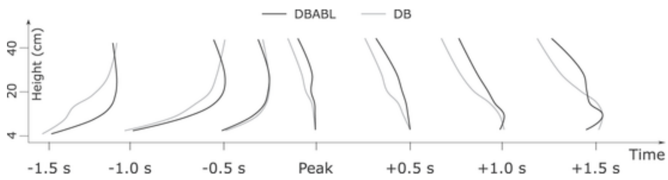

Fig. 16. Evolution of DB and DBABL radial velocity profiles at for at $\theta = 180°$ and $r/D = 1.5$ obtained from moving mean velocity records using a 0.3 s averaging window. Velocities are normalized with the maximum velocity, while the height (in cm) and time (in s) are not normalized.

ity records. Also, the time evolution of the heights of the maximum velocity is different between the DB and DBABL winds. The strongest winds in the DBABL outflow are closer to the surface than in the DB case during the ramp-up segment. Around the peak time, both wind systems have the maximum winds around the lowest measuring height or below. This height gradually increases during the ramp-down segment in both outflows. The smaller nose-shaped curvature in the DBABL winds during the ramp-down segment agrees with the numerical results in Mason et al. (2010) and the proposed conceptual model of the DBABL flow field (Fig. 12), in which the ABL winds hinder the full development of the primary vortex in the forward region of the outflow.

3.2. Spatial analysis of the DB and DBABL flow fields

Mean values of radial velocities ($\bar{u}$) in the steady-state segments of the DB and DBABL records at each measuring height were normalized against their respective downdraft center line velocities ($\bar{U}_j$) and plotted in Fig. 17 and Fig. 18, respectively. Linear interpolation was used to smooth the measurements on the rest of the polar plot. The DB outflow in the WindEEE Dome is symmetric around the downdraft center with the highest velocities occurring around $r/D = 1.0$. At this radial distance, the azimuthally averaged radial velocity in the DB outflow is $1.026\bar{U}_j$ at the height of $z/D = 0.0125$. The empirical model of Rajaratnam (1976, p. 235) predicts the value of $1.03\bar{U}_j$ based on the experimental results from Poreh et al. (1967). However, a slight asymmetry in the isolated DB outflow is also noticeable and already discussed in the previous section. Radial velocities at $\theta \geq 90°$ are slightly higher when compared to the rest of the outflow; particularly at $z/D = 0.0625$. However, the azimuthal differences of mean radial velocity at this height are below 7.7% everywhere in the measured outflow. This discrepancy is lower at the other five heights. The slight asymmetry in the near-surface DB outflow might be due to the observed irregularity of the downdraft velocity profiles in Fig. 2 that shows the slightly higher downdraft velocities in the region towards $\theta = 180°$. Notice in Fig. 2 that the DBABL downdrafts are more symmetric than DB jets along the cross-ABL wind direction.

When compared to the symmetric DB outflow with acknowledged irregularities in Fig. 17, the DBABL outflow is highly asymmetric around θ (Fig. 18). As expected, the high radial velocities are found in the forward region, while the weaker (outward) radial velocities are in the rear region of the outflow. At $\theta = 90°$, the radial velocities are like those observed in the DB case, but still slightly higher. The smallest decline of radial velocities with height is found in the forward region of the outflow, which is in accordance with the proposed outflow model in Fig. 12. The DBABL flow field at the height $z/D = 0.0469$ in Fig. 18

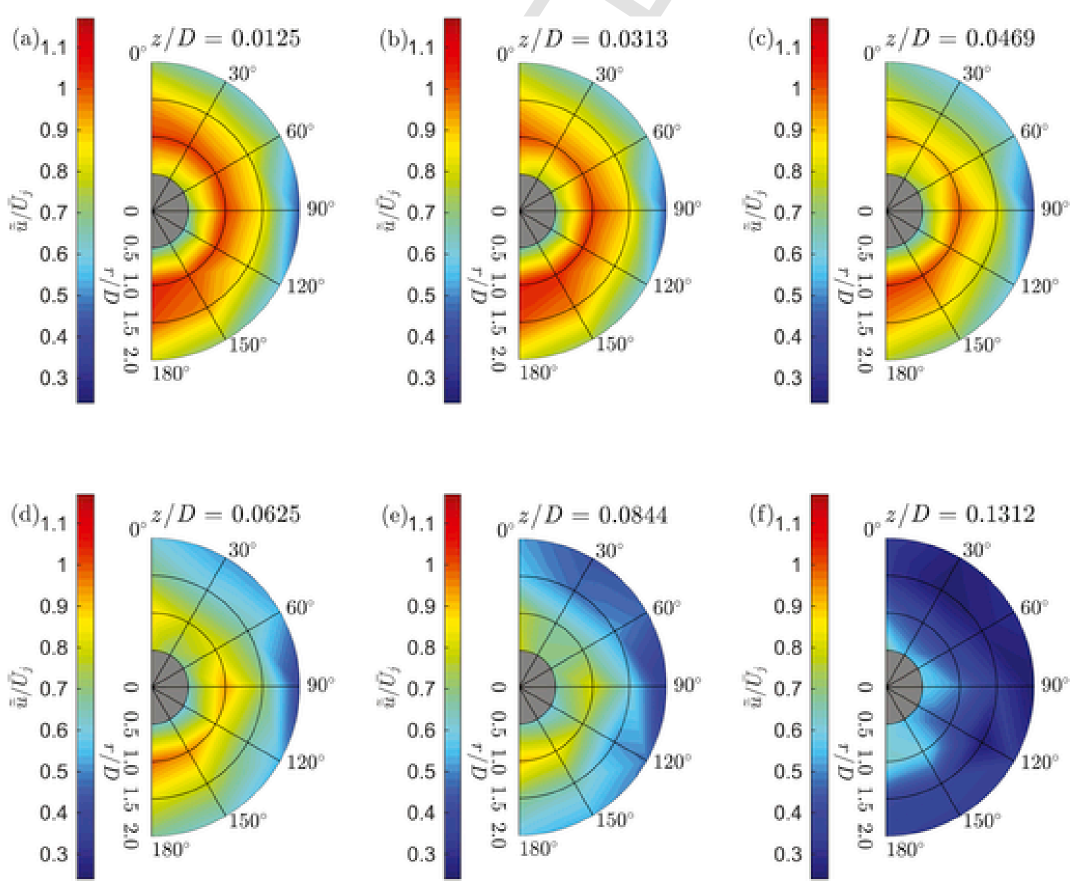

Fig. 17. The normalized ensemble mean radial (outward) velocities in the DB outflow during the steady impingement segment of velocity records. Radial distances (r/D) from the downdraft center and azimuth angles around the downdraft indicated in each plot. The grey region in the center indicates the absence of outward radial velocity measurements. The plots (a) to (f) indicate different measurement heights in the outflow.

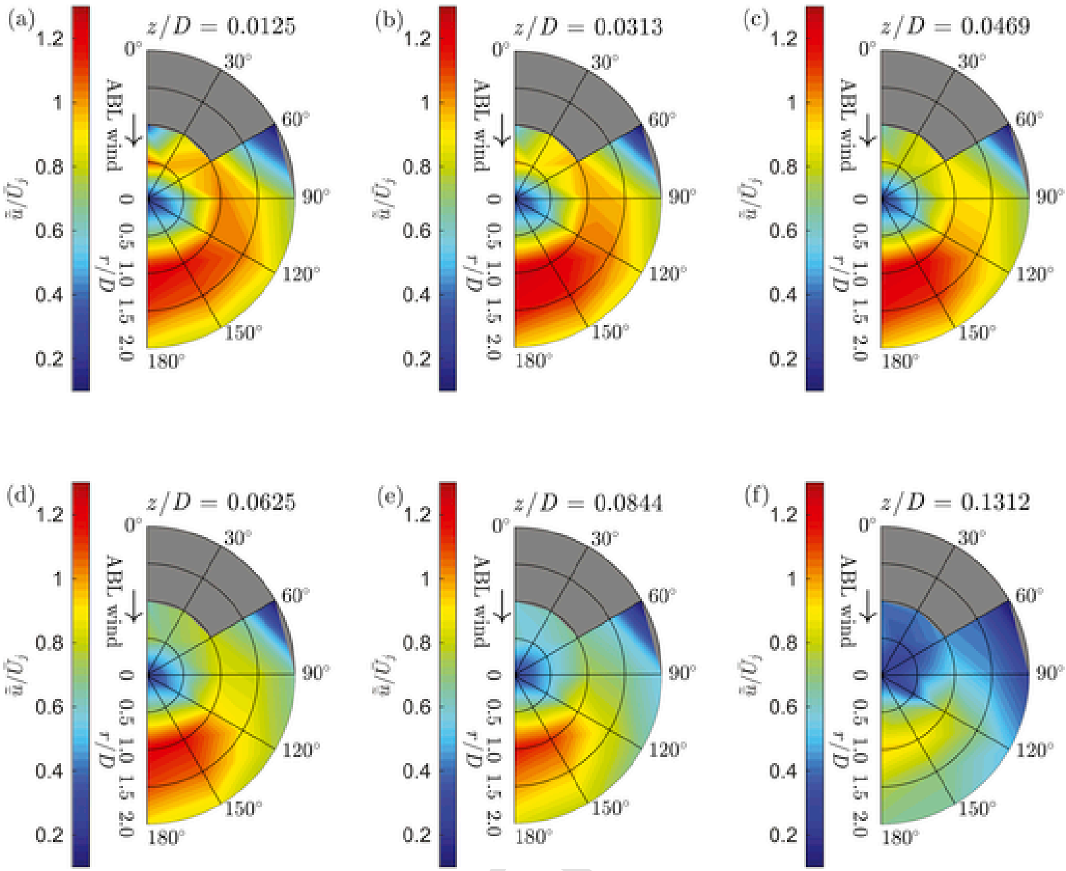

Fig. 18. The normalized ensemble mean radial (outward) velocities in the DBABL outflow during the steady impingement segment of velocity records. The grey region indicates the absence of reliable outward radial velocity measurements. The direction of ABL winds also included in each plot and the rest of notation as in Fig. 17.

agrees well with the reconstructed flow field of the New Orleans (Louisiana, US) microburst on July 9, 1982 from Fujita and Wakimoto (1983). Namely, in addition to the bean-shaped zone of the maximum velocities in the forward region—if the current observations are mirrored to the plain θ =[180°, 270°]—the ratio of velocities at $\theta = 180°$ and $\theta = 90°$ around $r/D = 1.0$ is approximately 1.5 in both cases. The same flow field pattern was found in the numerical study of traveling microbursts in background ABL winds by Orf and Anderson (1999). Their study also showed the absence of radially outward winds in the rear regions of the DBABL outflow (the grey zone in Fig. 18).

The turbulence intensity ($\widetilde{I}$) field in the DBABL outflow that was calculated as the ensemble mean of turbulence intensities ($I = \sigma_u/\bar{u}$) from four experiment repetitions is shown in Fig. 19. The highest turbulence is observed in the rear region of the outflow where the downburst is propagating against the ABL winds. The bean-shaped spatial distribution of the $\widetilde{I}$s is similar to the spatial pattern of mean velocities in Fig. 18. In addition to the high values of $\widetilde{I}$ in the rear region of the outflow, two other zones of high turbulence are found in the impingement zone of the downdraft and along the outflow periphery around $r/D = 2.0$. The higher values of $\widetilde{I}$ along the periphery of the DBABL outflow are in accordance with flow experiments of Barata and Durão (2004) that showed the existence of two counter-rotating vortices that form in the rear region and propagate along the direction of ABL winds on each side of the outflow. The flow structure in the vortices is similar to the horseshoe vortices that roll-up around bluff bodies due to boundary layer separation (Krothapalli et al., 1990; Kelso and Smits, 1995). Barata and Durão (2004) also demonstrated that the impingement zone is a highly turbulent region in the outflow. The high values of $\widetilde{I}$ at the highest measuring level ($z/D = 0.13125$) in the rear region of the outflow are probably due to the strong entrainment of ABL winds into the upper layers of the DBABL outflow.

Lastly, we investigate a ratio of enveloped radial velocity peaks in the DB and DBABL outflows ($\widehat{R}$) during the transient segment of the records defined as:

$$\widehat{R} = \frac{\widehat{u}_{DBABL}}{\widehat{u}_{DB}} \frac{U_{jet,DB}}{U_{jet,DBABL}}. \tag{4}$$

These transient segments are associated with the passage of the primary vortex over a measurement location. Fig. 20 shows an asymmetric footprint of $\widehat{R}$ around $r/D = 0$. Close to the surface (z/D<0.0625) and around r/D<0.5, the DBABL enveloped peaks are about 1.2 times larger than in the isolated DB case. Perhaps counterintuitive at first, but this zone is situated in the rear region of the outflow. A reason behind the higher velocity peaks in DBABL than in DB in this region of the outflow is discussed in Section 4.1 concerning Fig. 12. As the height increases, the zone of large $\widehat{R}$s is shifting towards the forward outflow region and around $\theta = 180°$. The largest speed-ups in the DBABL outflow from the DB case are observed at $\theta = 180°$ and at $r/D = 2.0$ or, perhaps, beyond this point, but those measurements were not conducted in the present study. These observations follow the conceptual model of flow interaction portrayed in Fig. 12. Namely, the increase of ABL winds with the height accelerates the upper regions of the DBABL outflow more than in the DB case. This stronger DBABL winds in the upper regions of the outflow at $\theta = 180°$ are also clearly demonstrated in the time-evolution of the radial velocity profiles in Fig. 16. Moreover, the stretching of the primary vortex and the increase of outflow depth in the forward region were also noticed by Mason et al. (2010) in their numerical work concerning DBABL outflows.

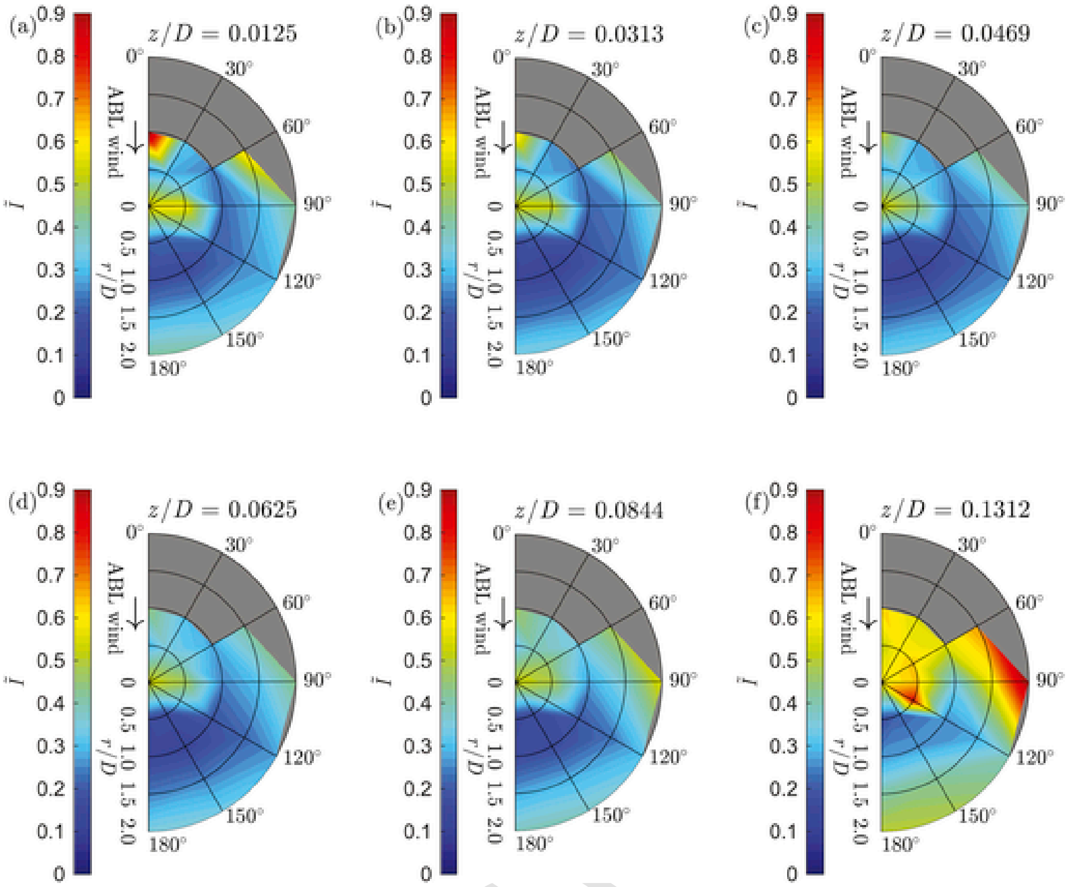

Fig. 19. Turbulence intensity of radial (outward) velocities ($\tilde{I}$) in the DBABL outflow during the steady impingement segment of velocity records. The rest of the notation as in Fig. 17.

3.3. Vector addition of the DB and ABL winds

The following analysis investigates if vector addition of the DB and ABL winds is satisfactory at representing the DBABL outflow. Simple models of vector addition of downburst translation and downburst outflow were previously used in Holmes and Oliver (2000), Chay et al. (2006), Kim and Hangan (2007), and Abd-Elaal et al. (2014). Letchford and Chay (2002) also proposed a simple model of vector addition of DB winds and cloud translation. In the present study, the starting hypothesis is:

$$\vec{X}_{\mathrm{DBABL}} = \vec{X}_{\mathrm{DB}} + \vec{X}_{\mathrm{ABL}}, \tag{5}$$

where $\vec{X}$ can be any velocity-related quantity. Here, we tested this hypothesis on the example of the mean radial velocities in the steady-state outflow, as well as the peak velocities in the primary vortex. A scalar form of Eq. (5) applied to the radial component of the DBABL winds (u_{DBABL}) is in the form:

$$u_{\mathrm{DBABL}} = u_{DB} - \cos\,\theta u_{\mathrm{ABL}}, \tag{6}$$

where u_{ABL} and u_{DB} are the ABL and DB velocities (mean or peak), respectively.

We further express Eq. (6) as a ratio:

$$\Lambda\left(\theta, r/D, z/D, t\right) = \frac{u_{\mathrm{DBABL}}}{u_{DB} - \cos\,\theta u_{\mathrm{ABL}}}. \tag{7}$$

Therefore, after replacing $\Lambda = \Lambda\left(\theta, r/D, z/D, t\right)$ for shortness, we observe that:

$$\Lambda = \begin{cases} = 1, & \text{The vector addition of DB and ABL winds is accurate,} \\ <1, & \text{DBABL overesimated using the vector addition of DB and ABL wi} \\ >1, & \text{DBABL underestimated using the vector addition of DB and ABL w} \end{cases}$$

The results of this analysis are shown in Fig. 21 for the enveloped radial velocity peaks in the primary vortex. Fig. 22 shows the ratio for the mean velocities in the steady-state segments of the two outflows. Overall, much of the flow field does not satisfy the hypothesis in Eq. (5) for the Λ-ratio of enveloped peaks ($\widehat{\Lambda}$) as well as means ($\bar{\Lambda}$). The enveloped peaks are predominantly overestimated using the vector addition of DB and DBABL winds. From the wind engineering point of view, this produces more conservative estimates of the wind loads, and the peak analysis is, therefore, "on the safe side." However, the zone of $\widehat{\Lambda}<1$ in the rear region of the outflow (around $r/D = 0.5$) shows a significant underestimation of the DBABL peaks. The vector addition produces enveloped peaks that are more than two times smaller than the observed values in the DBABL outflow.

The Λ-ratio of mean radial velocities in the steady-state segment of the records ($\bar{\Lambda}$) (Fig. 22) differs from the $\widehat{\Lambda}$ field (Fig. 21) by an increase of the region that undershoots the DBABL values. In addition to $\bar{\Lambda}<1$ in the rear region around $r/D = 0.5$, the $\bar{\Lambda}$ values are also below unity in the lateral sides of the outflow around $\theta = 90°$. This zone of $\bar{\Lambda}<1$ is more skewed towards the outer regions of the outflow. The experiments also show that the undershoot of the enveloped velocity peaks (Fig. 21) in DBABL is larger than the underestimation of the mean flow field (Fig. 22).

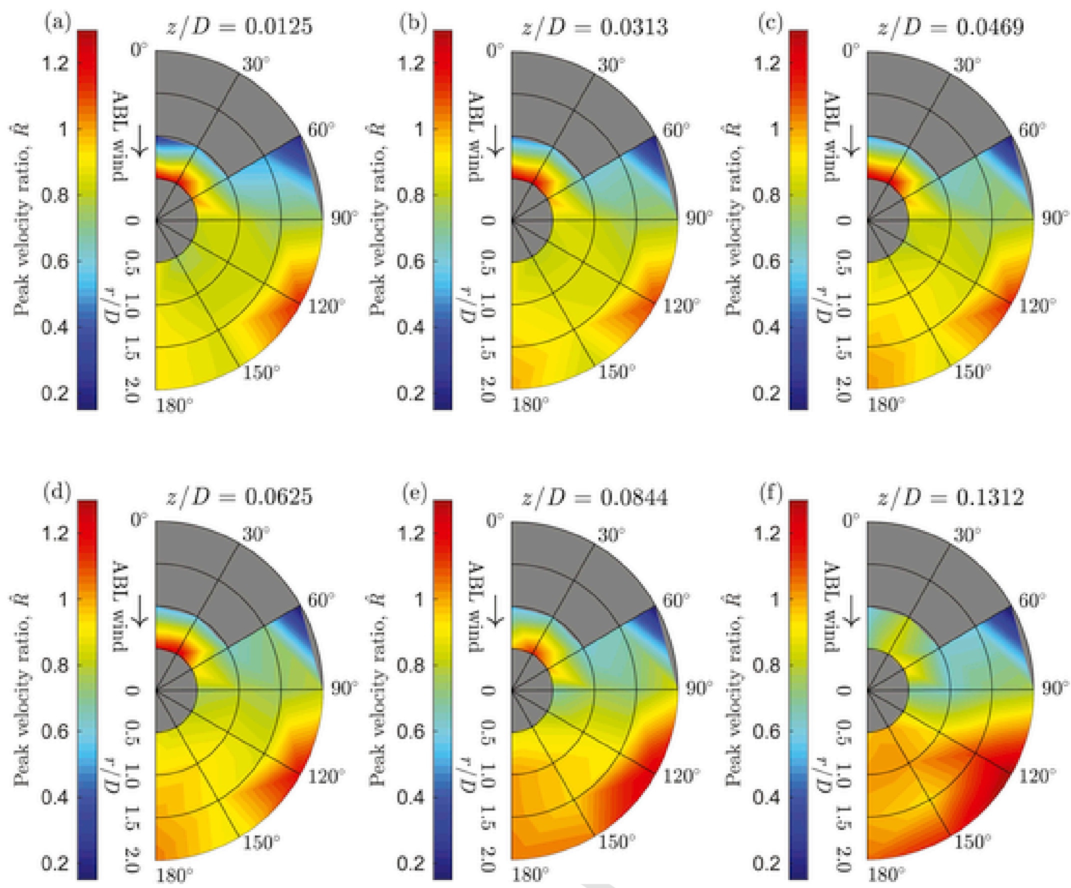

Fig. 20. The ratio of enveloped peak velocities in the DBABL and DB cases, $\hat{R}$. The rest of notation as in Fig. 17.

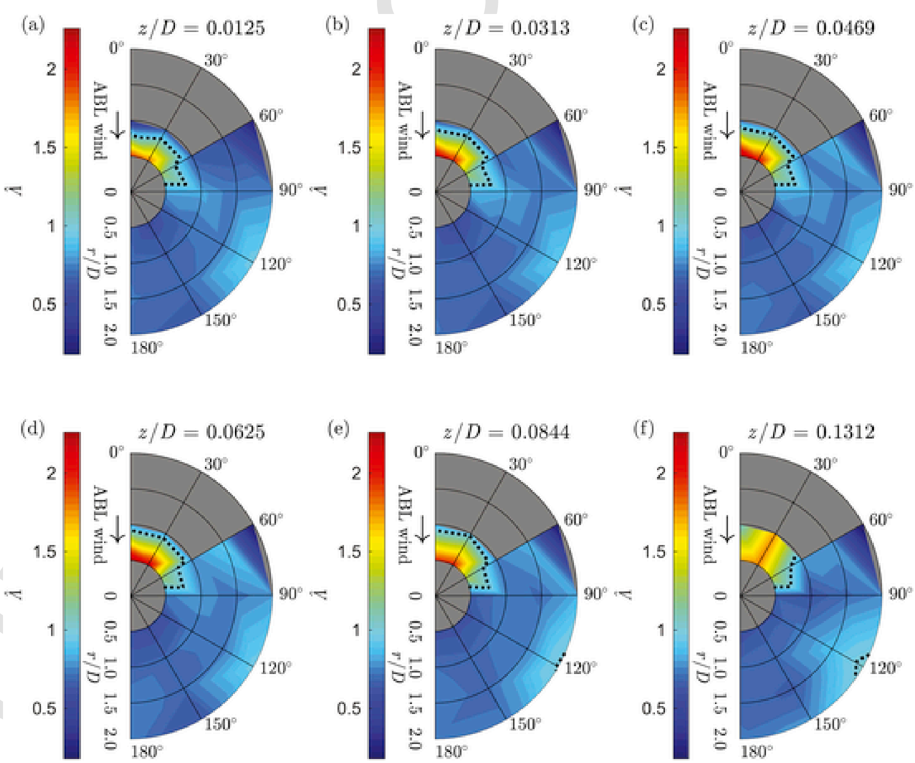

Fig. 21. The Λ ratio of enveloped peaks in the transient segment of the outflows ($\hat{\Lambda}$). The black dotted line shows $\hat{\Lambda} = 1$. The rest of the notation as in Fig. 17.

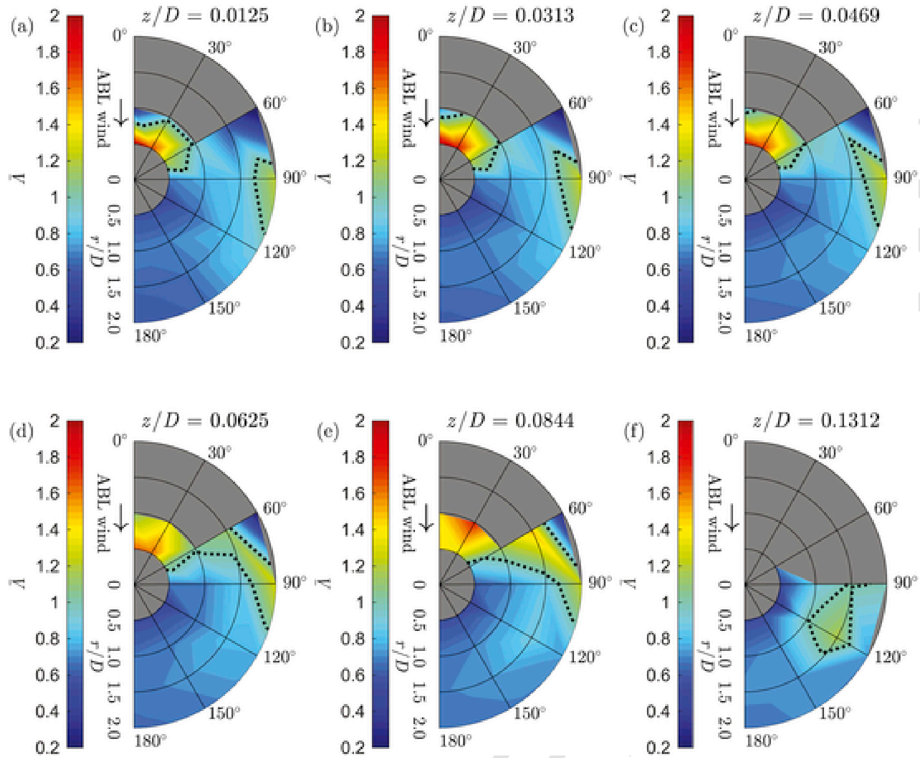

Fig. 22. The Λ ratio of mean radial velocities in the steady segment of the outflows ($\bar{\Lambda}$). The black dotted line shows $\bar{\Lambda} = 1$. The rest of the notation as in Fig. 17.

Considering that the rear region is also highly turbulent zone in the DBABL outflow (Fig. 19), the above underestimation of DBABL enveloped peaks calls for a caution when estimating the coupling of DB and DBABL winds in wind engineering. Wilson et al. (1984) and Mason et al. (2010) demonstrated that the vector addition of the downdraft and ABL winds seems to be a reasonable representation of the downdraft tilt angles, but Mason et al. (2010) still observed that more significant tilts were found in CFD simulation of DBABL flows than expected from the vector addition. Orf and Anderson (1999) also verified that the traveling microbursts in a unidirectional shear of ABL winds—such as the one produced in the current experiments—can augment the damaging near-surface winds compared to the isolated DB case.

3.4. A flow field comparison to real downburst

The present physical experiments are compared against a full-scale downburst event of July 8, 1982 (Hjelmfelt, 1988) that was measured during the JAWS field campaign that took place close to Denver, Colorado (US). The full-scale measurands were conducted using an S-band Doppler radar. In our study, Web Plot Digitizer (Rohatgi, 2019) was employed in digitizing the velocity data from Hjelmfelt (1988). The digitized and re-plotted velocity data are shown in Fig. 23a together with the wind directions at the cloud base ($\theta_{cb} = 240°$) and the surface ($\theta_{sfc} = 330°$). Due to this change of wind direction with height, we estimated the mean direction of background winds ($\theta_b = 276°$) as:

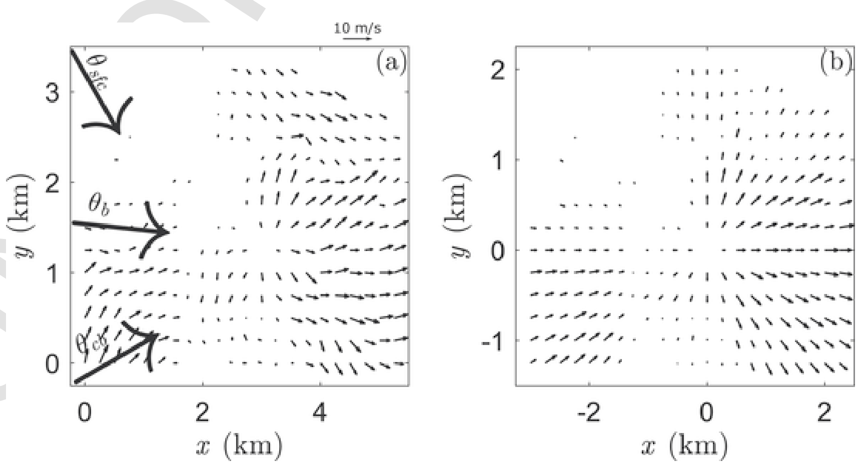

Fig. 23. (a) Digitized horizontal velocities from Hjelmfelt (1988) and the highlighted wind directions (not to scale) at cloud base (θ_{cb}), surface (θ_{sfc}) and the resulting direction of background wind (θ_b). (b) Radial velocity components measured from the estimated location of downdraft touchdown. The grid resolution is $\Delta x = \Delta y = 250$ m and the velocities were measured at approximately 200 m AGL.

$$\theta_b = \frac{u_{sfc}\theta_{sfc} + u_{cb}\theta_{cb}}{u_{sfc} + u_{cb}}, \tag{9}$$

where u_{cb} and u_{sfc} are the horizontal wind speeds at cloud base and surface, respectively, and θ_{sfc} and θ_{cb} are their respective wind directions (in °). The wind speeds in Eq. (9) serve as weighting factors with the values of $u_{sfc} = 4$ m s^{-1} and $u_{cb} = 6$ m s^{-1}. The cloud base was at 2600 m above ground level (AGL), and the thunderstorm was a multicell cumulonimbus cloud with pronounced virga (Hjelmfelt, 1988). The uncertainty of horizontal velocity measurements in Hjelmfelt (1988) was about 2 m s^{-1} (Wilson et al., 1984). The radar-resolved flow field and velocity profile retrievals are less accurate than anemometer measurements (Gunter et al., 2015). Also, as a side note, θ_{sfc} and u_{sfc} are measured at 10 m AGL in the standard meteorological practice.

Next, the horizontal velocities in Fig. 23a are converted from the Cartesian coordinates to polar coordinates reference frame as:

$$\begin{pmatrix} u \\ v \end{pmatrix} = \begin{pmatrix} \cos\theta & \sin\theta \\ -\sin\theta & \cos\theta \end{pmatrix} \begin{pmatrix} u_c \\ v_c \end{pmatrix} \tag{10}$$

where u_c and v_c are the Cartesian wind speed components, and θ is the azimuth angle in polar coordinates. The radial velocity components (u) in the polar coordinate system with the origin at the estimated downburst impingement location are shown in Fig. 23b.

The geometric and velocity scales of DB outflows in the WindEEE Dome were discussed in Junayed et al. (2019) and Hangan et al. (2019), and, more recently, by Romanic et al. (2020) in the comprehensive study of DB scales and DB scaling methodology. With the full-scale downdraft diameter of $D_p = 1400$ m (Hjelmfelt, 1988), the measurement height of horizontal velocities in Fig. 23 is at $z_p/D_p = 0.143$ (the subscript "p" stands for the "prototype"). This non-dimensional height is close to $z_m/D_m = 0.131$ (the subscript "m" stands for the "model") in the present physical experiments (9.2% of the height difference). Thus, the derived geometric scale between the p event in Fig. 23 and the m measurements in the WindEEE Dome is: $D_p/D_m = 1400/3.2 = 437.5 \cong 450$ (i.e., 1:450 if the scale is defined as the m diameter over the p dimeter). The estimated scale corroborates well with the range of geometric scales of the WindEEE Dome downbursts in Romanic et al. (2020) and Junayed et al. (2019). However, we do acknowledge that other, more sophisticated, scaling methodologies could be used to assess the relationship between the p and m events.

To account for the cloud base height (H) and downburst diameter (D), velocities in both p and m outflows were normalized as (Gutmark et al., 1978; Ho and Nosseir, 1981):

$$u_{ref,s} = \hat{\bar{u}}_s \sqrt{\frac{D_s}{H_s}}, \tag{11}$$

where $s = p$ or m. The comparison between the m and p flow fields is performed over the steady-state segment of the m records and $\hat{\bar{u}}_m$ in Eq. (11) represents the maximum of the mean velocity in the entire outflow at $z_m/D_m = 0.131$. The obtained values of $u_{ref,p}$ and $u_{ref,m}$ are 5.43 m s^{-1} and 5.96 m s^{-1}, respectively.

The simple geometric scaling employed in this study results in the same range of r/D values of full-scale and experimental data in Fig. 24. The highest normalized velocities in the p and m events are found between $r_s/D_s = 1.0$ and $r_s/D_s = 1.5$ in the forward region on the outflows. In addition, there is a good overall similarity between the entire spatial footprint of two outflows. The negative radial velocities that are observed in the side and rear regions of the p event are not measured in the current DBABL experiment partially due to the orientation of the Cobra probes (Fig. 4) and partially due to the discrepancies between the p and m flow fields in these regions. That is, the physical experiments are still an idealized representation of real events, and the current setup does not account for cloud translation and various other factors such as surface roughness, orography, and atmospheric stability. While the cloud translation, roughness changes, and orography can be added to this experimental setup in the future, the WindEEE Dome simulator was not designed to produce gravity currents and different thermal stability regimes in the outflow. Despite this idealized nature of the experiments, the range of normalized velocities and radial distances in Fig. 24 is the same between the two outflows. We also emphasize that this asymmetric, bean-shaped outflow cannot be produced in an m experiment of isolated DB.

This flow field pattern was also found in numerical simulations of Orf and Anderson (1999) and Mason et al. (2010). The simulated outflow in Fig. 24a is further similar to a case of translating downburst. This similarity suggests that the DBABL outflows might produce equivalent flow field to a translating downburst generated without background ABL winds, but additional tests are needed to confirm this proposal. Therefore, the importance of present physical experiments of DBABL winds and above numerical studies that all corroborate well with the full-scale data is of great importance in downburst wind engineering. While we also acknowledge some of the discrepancies between the m and p flow fields in Fig. 24, the presented analysis is the best that currently can be accomplished with limited full-scale and experimental data.

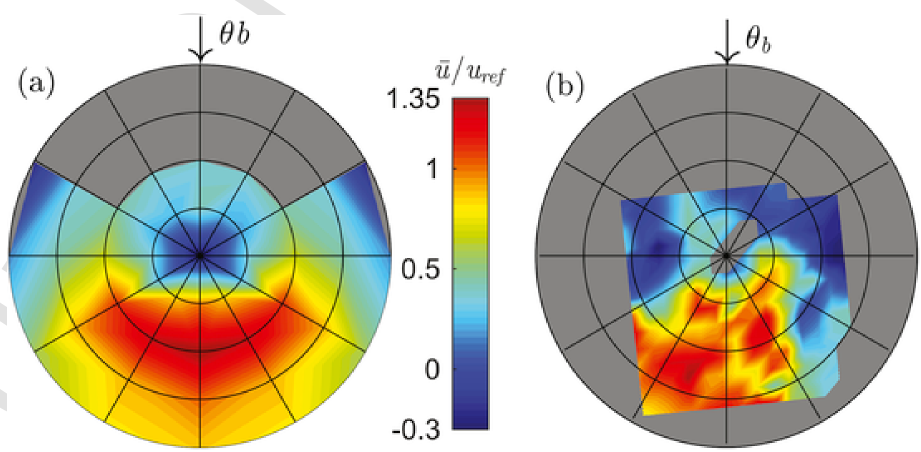

Fig. 24. Normalized radial velocities at (a) $z_m/D_m = 0.131$ in the DBABL outflow in the WindEEE Dome; and (b) $z_p/D_p = 0.143$ in the real downburst event from the JAWS Project (see Fig. 23b). Both plots are aligned along the direction of background ABL wind (θ_b; black arrow).

4. Conclusions and outlook

The research presented in this paper investigates the interplay between near-surface atmospheric boundary layer (ABL) winds and downburst outflows. The study was based on a set of physical experiments carried out inside the Wind Engineering, Energy and Environment (WindEEE) Dome downburst simulator at Western University in Canada. The coupling between downburst and ABL winds was investigated for five different radial distances from the undisturbed downdraft center (r/D), seven different azimuth angles (θ) in respect to the incoming ABL winds, and six different heights above the floor (z/D). Here, r, z, and $D = 3.2$ m are dimensional radial distance, height, and downdraft diameter, respectively. In this notation, $\theta = 0°$, $90°$, and $180°$ depict the azimuthal directions in which the radially propagating downburst outflows and the streamwise component of ABL winds are in the opposite, perpendicular, and same directions, respectively. This study also introduced a methodology for the segmentation of velocity records of physically produced downburst into transient and steady-state parts.

We demonstrated through a series of different analyses that isolated downbursts (DB; i.e., downbursts without background ABL winds) and DBABL downbursts (i.e., downbursts immersed into background ABL winds) are profoundly different in terms of mean and peak velocities, as well as turbulence intensities. The discrepancies between the two outflows highly depend on r/D, θ, z/D, and time (t).

The study also demonstrated that the vector addition of downburst radial velocities and ABL winds is inaccurate throughout the flow field, i.e.:

$$\overline{\mathrm{DBABL}} \neq \overline{\mathrm{DB}} + \overline{\mathrm{ABL}}. \tag{12}$$

In some regions of the DBABL outflow, this simple vector addition of DB and ABL winds produces enveloped peaks that are more than two times smaller than the observed values in the DBABL outflow. Moreover, this region of peak underestimation is situated in the highly turbulent part of the DBABL outflow.

This study also compared the enveloped peak and instantaneous maximum radial velocity profiles in the DBABL outflow to several Doppler radar measurements of real thunderstorm winds from the US (Fujita, 1981; Hjelmfelt, 1988; Gunter and Schroeder, 2015) and Australia (Sherman, 1987). The similarity between enveloped peaks in the experiments and reality is higher than the similarity between the instantaneous profiles in the outflows. The results were also benchmarked against numerical simulations of DBABL winds in Mason et al. (2010), and qualitatively discussed concerning the numerical simulations in Orf and Anderson (1999). Moreover, the entire DBABL flow field was compared against the real downburst outflows from Hjelmfelt (1988). The experimentally produced DBABL flow field showed the beam-shape spatial pattern similar to that of the real downburst from Hjelmfelt (1988). Furthermore, a discussion of the produced DBABL flow field in relation to the real near-surface downburst winds from Fujita and Wakimoto (1983) was also included. The overall resemblance between the experiments and reality warrants high fidelity results.

Lastly, this research also serves as an initial point for a series of future studies that will be devoted to this subject. The DBABL outflow dynamics that result from different intensities of isolated DB and ABL winds (Romanic et al., 2019), including a variety of different ABL wind profiles, should be investigated in order to generalize the results of this study. Also, an experimental work that will consider translating downdrafts with and without ABL winds should be conducted to assess the importance of these factors to downburst outflow dynamics. Some of the uncertainties from this research should also be addressed in future work. For example, a deflection of the DBABL downdraft from the location $r/D = 0$ of the isolated DB should be quantified for different strengths of the DBABL downdrafts.

Author contributions

Djordje Romanic: Conceptualization, Methodology, Software, Data curation, Writing—Original draft preparation, Visualization, Investigation. Horia Hangan: Supervision, Writing—Editing and Reviewing, Project administration, Funding acquisition, Resources.

Declaration of competing interest

The authors declare that they have no known competing financial interests or personal relationships that could have appeared to influence the work reported in this paper.

f

Acknowledgment

The first author acknowledges partial support from the European Research Council (ERC) under the European Union's Horizon 2020 research and innovation program (grant agreement No. 741273) for the project THUNDERR (Detection, simulation, modelling and loading of thunderstorm outflows to design wind-safer and cost-efficient structures), awarded with an Advanced Grant 2016. The authors would like to thank Mr. Julien LoTufo and Mr. Gerald Dafoe for their technical help in preparing and conducting the experiments in the WindEEE Dome. We also thank Mr. Dan Parvu for his help with MATLAB® coding and preparation of Fig. 12. The authors thank Mr. Clement Rouaix for his help in digitizing some of the velocity data that were used in Section 5. We acknowledge constructive comments from four anonymous reviewers that substantially improved the quality of this work.

References

Abd-Elaal, E-S, Mills, J E, Ma, X, 2014. Empirical models for predicting unsteady-state downburst wind speeds. J. Wind Eng. Ind. Aerod. 129, 49–63. doi:10.1016/j.jweia.2014.03.011.

Anderson, J R, Orf, L G, Straka, J M, 1992. A 3-D modelsyystem for simulating thunderstorm microburst outflows. Meteorl Atmos Phys 49, 125–131. doi:10.1007/BF01025404.

Asano, K, Iida, Y, Uematsu, Y, 2019. Laboratory study of wind loads on a low-rise building in a downburst using a moving pulsed jet simulator and their comparison with other types of simulators. J. Wind Eng. Ind. Aerod. 184, 313–320. doi:10.1016/j.jweia.2018.11.034.

Barata, J M M, Durão, D F G, 2004. Laser-Doppler measurements of impinging jet flows through a crossflow. Exp. Fluid 36, 665–674. doi:10.1007/s00348-003-0737-3.

Bunkers, M J, Klimowski, B A, Zeitler, J W, et al., 2000. Predicting supercell motion using a new hodograph technique. Weather Forecast. 15, 61–79. doi:10.1175/1520-0434(2000)015 < 0061:PSMUAN > 2.0.CO;2.

Burlando, M, Romanić, D, Solari, G, et al., 2017. Field data analysis and weather scenario of a downburst event in Livorno, Italy, on 1 October 2012. Mon. Weather Rev. 145, 3507–3527. doi:10.1175/MWR-D-17-0018.1.

Burlando, M, Zhang, S, Solari, G, 2018. Monitoring, cataloguing, and weather scenarios of thunderstorm outflows in the northern Mediterranean. Nat. Hazards Earth Syst. Sci. 18, 2309–2330. doi:10.5194/nhess-18-2309-2018.

Businger, J A, Wyngaard, J C, Izumi, Y, Bradley, E F, 1971. Flux-profile relationships in the atmospheric surface layer. J. Atmos. Sci. 28, 181–189. doi:10.1175/1520-0469(1971)028 < 0181:FPRITA > 2.0.CO;2.

Charba, J, 1974. Application of gravity current model to analysis of squall-line gust front. Mon. Weather Rev. 102, 140–156. doi:10.1175/1520-0493(1974)102 < 0140:AOGCMT > 2.0.CO;2.

Chay, M T, Albermani, F, Wilson, R, 2006. Numerical and analytical simulation of downburst wind loads. Eng. Struct. 28, 240–254. doi:10.1016/j.engstruct.2005.07.007.

Chay, M T, Letchford, C W, 2002. Pressure distributions on a cube in a simulated thunderstorm downburst—Part A: stationary downburst observations. J. Wind Eng. Ind. Aerod. 90, 711–732. doi:10.1016/S0167-6105(02)00158-7.

Choi, E C C, 2004. Field measurement and experimental study of wind speed profile during thunderstorms. J. Wind Eng. Ind. Aerod. 92, 275–290. doi:10.1016/j.jweia.2003.12.001.

De Gaetano, P, Repetto, M P, Repetto, T, Solari, G, 2014. Separation and classification of extreme wind events from anemometric records. J. Wind Eng. Ind. Aerod. 126, 132–143. doi:10.1016/j.jweia.2014.01.006.

Demuren, A O, 1994. Modeling Jets in Cross Flow. Institute for Computer Applications in Science and Engineering, NASA Langley Research Center, Hampton, VA.

Droegemeier, K K, Wilhelmson, R B, 1987. Numerical simulation of thunderstorm outflow dynamics. Part I: outflow sensitivity experiments and turbulence dynamics. J. Atmos. Sci. 44, 1180–1210. doi:10.1175/1520-0469(1987)044<1180:NSOTOD>2.0.CO;2.

ESDU, 2002. Characteristics of Atmospheric Turbulence Near the Ground. Part 2: Single Point Data for Strong Winds (Neutral Atmosphere). ESDU International PLC, London.

Fairweather, M, Hargrave, G, 2002. Experimental investigation of an axisymmetric, impinging turbulent jet. 1. Velocity field. Exp. Fluid 33, 464–471. doi:10.1007/s00348-002-0479-7.

Fric, T F, Roshko, A, 1994. Vortical structure in the wake of a transverse jet. J. Fluid Mech. 279, 1–47. doi:10.1017/S0022112094003800.

Fujita, T T, 1990. Downbursts: meteorological features and wind field characteristics. J. Wind Eng. Ind. Aerod. 36, 75–86. doi:10.1016/0167-6105(90)90294-M.

Fujita, T T, 1981. Tornadoes and downbursts in the context of generalized planetary scales. J. Atmos. Sci. 38, 1511–1534. doi:10.1175/1520-0469(1981)038<1511:TADITC>2.0.CO;2.

Fujita, T T, Wakimoto, R M, 1983. Microbursts in JAWS Depicted by Doppler Radars, PAM, and Aerial Photographs. American Meteorological Society, Edmonton, Alberta, Canada, pp. 638–645.

Gromke, C, Ruck, B, 2015. PIV-measurements on the momentum transfer in the forest edge region during extreme gusts. Proceedings der 24. Fachtagung Experimentelle Strömungsmechanik. pp. 1–10 Cottbus, Germany, B37.

Gunter, W S, Schroeder, J L, 2015. High-resolution full-scale measurements of thunderstorm outflow winds. J. Wind Eng. Ind. Aerod. 138, 13–26. doi:10.1016/j.jweia.2014.12.005.

Gunter, W S, Schroeder, J L, Hirth, B D, 2015. Validation of dual-Doppler wind profiles with in situ anemometry. J. Atmos. Ocean. Technol. 32, 943–960. doi:10.1175/JTECH-D-14-00181.1.

Guo, Y, Wood, D H, 2001. Instantaneous velocity and pressure measurements in turbulent mixing layers. Exp. Therm. Fluid Sci. 24, 139–150. doi:10.1016/S0894-1777(01)00046-2.

Gutmark, E, Wolfshtein, M, Wygnanski, I, 1978. The plane turbulent impinging jet. J. Fluid Mech. 88, 737–756. doi:10.1017/S0022112078002360.

Hangan, H, 2010. Current and future directions for wind research at Western: a new quantum leap in wind research through the Wind Engineering, Energy and Environment (WindEEE) Dome. Wind Engineers, JAWE 35, 277–281. doi:10.5359/jawe.35.277.

Hangan, H, Refan, M, Jubayer, C, et al., 2017. Novel techniques in wind engineering. J. Wind Eng. Ind. Aerod. 171, 12–33. doi:10.1016/j.jweia.2017.09.010.

Hangan, H, Romanic, D, Jubayer, C, 2019. Three-dimensional, non-stationary and non-Gaussian (3D-NS-NG) wind fields and their implications to wind–structure interaction problems. J Fluid Struct In press. doi:10.1016/j.jfluidstructs.2019.01.024.

Hjelmfelt, M R, 1988. Structure and life cycle of microburst outflows observed in Colorado. J. Appl. Meteorol. 27, 900–927. doi:10.1175/1520-0450(1988)027<0900:SALCOM>2.0.CO;2.

Ho, C-M, Nosseir, N S, 1981. Dynamics of an impinging jet. Part 1. The feedback phenomenon. J. Fluid Mech. 105, 119–142. doi:10.1017/S0022112081003133.

Holmes, J D, Oliver, S E, 2000. An empirical model of a downburst. Eng. Struct. 22, 1167–1172. doi:10.1016/S0141-0296(99)00058-9.

Järvi, L, Punkka, A-J, Schultz, D M, et al., 2007. Micrometeorological observations of a microburst in southern Finland. Boundary-Layer Meteorol. 125, 343–359. doi:10.1007/s10546-007-9204-7.

Jubayer, C, Romanic, D, Hangan, H, 2019. Aerodynamic loading of a typical low-rise building for an experimental stationary and non-Gaussian impinging jet. Wind Struct. 28, 315–329. doi:10.12989/was.2019.28.5.315.

Junayed, C, Jubayer, C, Parvu, D, et al., 2019. Flow field dynamics of large-scale experimentally produced downburst flows. J. Wind Eng. Ind. Aerod. 188, 61–79. doi:10.1016/j.jweia.2019.02.008.

Kamotani, Y, Greber, I, 1972. Experiments on a turbulent jet in a cross flow. AIAA J. 10, 1425–1429. doi:10.2514/3.50386.

Karagozian, A R, 2014. The jet in crossflow. Phys. Fluids 26, 101303. doi:10.1063/1.4895900.

Kelso, R M, Smits, A J, 1995. Horseshoe vortex systems resulting from the interaction between a laminar boundary layer and a transverse jet. Phys. Fluids 7, 153–158. doi:10.1063/1.868736.

Killick, R, Fearnhead, P, Eckley, I A, 2012. Optimal detection of changepoints with a linear computational cost. J. Am. Stat. Assoc. 107, 1590–1598. doi:10.1080/01621459.2012.737745.

Kim, J, Hangan, H, 2007. Numerical simulations of impinging jets with application to downbursts. J. Wind Eng. Ind. Aerod. 95, 279–298. doi:10.1016/j.jweia.2006.07.002.

Krothapalli, A, Lourenco, L, Buchlin, J M, 1990. Separated flow upstream of a jet in a crossflow. AIAA J. 28, 414–420. doi:10.2514/3.10408.

Lavielle, M, 2005. Using penalized contrasts for the change-point problem. Signal Process. 85, 1501–1510. doi:10.1016/j.sigpro.2005.01.012.

Letchford, C W, Chay, M T, 2002. Pressure distributions on a cube in a simulated thunderstorm downburst. Part B: moving downburst observations. J. Wind Eng. Ind. Aerod. 90, 733–753. doi:10.1016/S0167-6105(02)00163-0.

Letchford, C W, Mans, C, Chay, M T, 2002. Thunderstorms—their importance in wind engineering (a case for the next generation wind tunnel). J. Wind Eng. Ind. Aerod. 90, 1415–1433. doi:10.1016/S0167-6105(02)00262-3.

Lompar, M, Ćurić, M, Romanic, D, 2018. Implementation of a gust front head collapse scheme in the WRF numerical model. Atmos. Res. 203, 231–245. doi:10.1016/j.atmosres.2017.12.018.

Mahesh, K, 2013. The interaction of jets with crossflow. Annu. Rev. Fluid Mech. 45, 379–407. doi:10.1146/annurev-fluid-120710-101115.

Mahoney, W P, 1988. Gust front characteristics and the kinematics associated with interacting thunderstorm outflows. Mon. Weather Rev. 116, 1474–1492. doi:10.1175/1520-0493(1988)116<1474:GFCATK>2.0.CO;2.

Markowski, P, Richardson, Y, 2010. Mesoscale Meteorology in Mid-latitudes. John Wiley & Sons, Ltd, Chichester, United Kingdom.

Markowski, P M, Lis, N T, Turner, D D, et al., 2019. Observations of ear-surface vertical wind profiles and vertical momentum fluxes from VORTEX-SE 2017: comparisons to Monin–Obukhov similarity theory. Mon. Weather Rev. 147, 3811–3824. doi:10.1175/MWR-D-19-0091.1.

Mason, M S, Fletcher, D F, Wood, G S, 2010. Numerical simulation of idealised three-dimensional downburst wind fields. Eng. Struct. 32, 3558–3570. doi:10.1016/j.engstruct.2010.07.024.

Mason, M S, Wood, G S, Fletcher, D F, 2009. Numerical simulation of downburst winds. J. Wind Eng. Ind. Aerod. 97, 523–539. doi:10.1016/j.jweia.2009.07.010.

McConville, A C, Sterling, M, Baker, C J, 2009. The physical simulation of thunderstorm downbursts using an impinging jet. Wind Struct. 12, 133–149. doi:10.12989/was.2009.12.2.133.

Muppidi, S, Mahesh, K, 2005. Study of trajectories of jets in crossflow using direct numerical simulations. J. Fluid Mech. 530, 81–100. doi:10.1017/S0022112005003514.

Nieuwstadt, F, 1978. The computation of the friction velocity u*and the temperature scale T*from temperature and wind velocity profiles by least-square methods. Boundary-Layer Meteorol. 14, 235–246. doi:10.1007/BF00122621.

Orf, L G, Anderson, J R, 1999. A numerical study of traveling microbursts. Mon. Weather Rev. 127, 1244–1258. doi:10.1175/1520-0493(1999)127<1244:ANSOTM>2.0.CO;2.

Poreh, M, Tsuei, Y G, Cermak, J E, 1967. Investigation of a turbulent radial wall jet. J. Appl. Mech. 34, 457–463. doi:10.1115/1.3607705.

Proctor, F H, 1988. Numerical simulations of an isolated microburst. Part II: sensitivity experiments. J. Atmos. Sci. 46, 2143–2165. doi:10.1175/1520-0469(1989)046<2143:NSOAIM>2.0.CO;2.

Rajaratnam, N, 1976. Turbulent Jets. first ed. Elsevier, Amsterdam, The Netherlands.

Richter, A, Ruck, B, Mohr, S, Kunz, M, 2018. Interaction of severe convective gusts with a street canyon. Urban Climate 23, 71–90. doi:10.1016/j.uclim.2016.11.003.

A. Rohatgi WebPlotDigitalizer: HTML5 based online tool to extract numerical data from plot imagesVersion 4.2https://apps.automeris.io/wpd/20196 July 2019

Romanic, D, Junayed, C, Jubayer, C, Hangan, H, 2020. Investigation of the transient nature of thunderstorm winds from Europe, United States and Australia using a new method for detection of changepoints in wind speed records. Mon. Weather Rev.. doi:10.1175/MWR-D-19-0312.1.

Romanic, D, LoTufo, J, Hangan, H, 2019. Transient behavior in impinging jets in crossflow with application to downburst flows. J. Wind Eng. Ind. Aerod. 184, 209–227. doi:10.1016/j.jweia.2018.11.020.

Romanic, D, Nicolini, E, Hangan, H, et al., 2020. A novel approach to scaling experimentally produced downburst-like impinging jet outflows. J. Wind Eng. Ind. Aerod. 196, 104025. doi:10.1016/j.jweia.2019.104025.

Sengupta, A, Sarkar, P P, 2008. Experimental measurement and numerical simulation of an impinging jet with application to thunderstorm microburst winds. J. Wind Eng. Ind. Aerod. 96, 345–365. doi:10.1016/j.jweia.2007.09.001.

Sherman, D J, 1987. The passage of a weak thunderstorm downburst over an instrumented tower. Mon. Weather Rev. 115, 1193–1205. doi:10.1175/1520-0493(1987)115<1193:TPOAWT>2.0.CO;2.

Skote, M, Sim, T S, Srikanth, N, 2018. Temporal variation of the pressure from a steady impinging jet model of dry microburst-like wind using URANS. Computation 6, 2. doi:10.3390/computation6010002.

Wakimoto, R M, 1982. The life cycle of thunderstorm gust fronts as viewed with Doppler radar and rawinsonde data. Mon. Weather Rev. 110, 1060–1082. doi:10.1175/1520-0493(1982)110<1060:TLCOTG>2.0.CO;2.

Wilson, J W, Roberts, R D, Kessinger, C, McCarthy, J, 1984. Microburst wind structure and evaluation of Doppler radar for airport wind shear detection. J. Clim. Appl. Meteorol. 23, 898–915. doi:10.1175/1520-0450(1984)023<0898:MWSAEO>2.0.CO;2.

Wu, J M, Vakili, A D, Yu, F M, 1988. Investigation of the interacting flow of nonsymmetric jets in crossflow. AIAA J. 26, 940–947. doi:10.2514/3.9994.

Xu, Z, Hangan, H, 2008. Scale, boundary and inlet condition effects on impinging jets. J. Wind Eng. Ind. Aerod. 96, 2383–2402. doi:10.1016/j.jweia.2008.04.002.

Zhang, S, Solari, G, De Gaetano, P, et al., 2018. A refined analysis of thunderstorm outflow characteristics relevant to the wind loading of structures. Probabilist. Eng. Mech. 54, 9–24. doi:10.1016/j.probengmech.2017.06.003.